DEVELOPMENT OF A VISCOELASTIC CELLULAR MODEL TO ESTIMATE FORCES AT THE CELLULAR LENGTH SCALE

A Thesis

Presented to the Faculty of the Graduate School

of Cornell University

in Partial Fulfillment of the Requirements for the Degree of

Master of Science

by

Ankit Chandra

August 2014

ABSTRACT

Computational tools were developed to estimate extracellular and subcellular forces in a single cell (or a small population of cells) when it is subjected to external forces such as due to blast waves traversing through tissue and the subsequent formation and rupture of cavitation bubbles. To this effect the ability to capture the shape (or geometry) of cells and nuclei of regular-shaped cells (e.g. HL60 cells) and irregular-shaped cells (e.g. astrocytes) from images was developed. The resulting geometries of the cytoplasm and the nucleus were meshed with different meshing characteristics which were used to create a viscoelastic model of a cell. To create the viscoelastic model, the edges connecting the mesh point were replaced with Voigt elements. An open source software package was developed, which automatically generates a system of coupled ODEs with inequality constraints describing the kinematic response of the viscoelastic model to an external force. A Viscoelastic model of an HL60 cell embedded in an extracellular matrix was developed. The model had 1871 nodes which resulted in a system of 7484 coupled ODEs with inequality constraints. Forces in any part of the model could be estimated as a result of perturbations. A viscoelastic model for an astrocyte was also developed. In order to create an accurate viscoelastic model of a cell, the Voigt parameters need to be estimated from experimental data. An optimization procedure was created to develop the ability to estimate parameters from experimental data. These computational tools will aid in future studies to correlate forces at the cellular length scale with cellular signaling data to develop a mechanically coupled signal transduction network for secondary injury following mild traumatic brain injury.

BIOGRAPHICAL SKETCH

Ankit Chandra was born in Kanpur, India. He completed his primary and secondary education in Botswana and came to the United States for his undergraduate education. He received a Bachelor of Science (Hons) degree in Chemical Engineering with a minor in Theater from Lafayette College (Easton, PA) in 2012. Upon completing his undergraduate education, he joined the group of Dr. Jeffrey Varner at Cornell University as a graduate student and is currently working towards his PhD.

ACKNOWLEDGEMENTS

I would first like to thank Professor Varner for allowing me to work in the Varner Lab and for his continued support and encouragement. I would also like to thank my committee members Professor Clancy and Professor Butcher. Lastly, I would like to thank my fellow Varner lab members and my colleagues in the department of Chemical and Biomolecular Engineering.

TABLE OF CONTENTS

LIST OF FIGURES

CHAPTER 1

INTRODUCTION

Traumatic Brain Injury (TBI) is a leading cause of morbidity and death in both industrialized and developing countries [1, 2, 12]. TBI does not only occur through direct impact, such as in a car accident, but can also occur through indirect physical trauma, for example as a result of a blast wave. In the last 10 years the number of military personnel diagnosed with TBI has risen dramatically, mainly as a result of improvised explosive devices (IEDs) used in Afghanistan and Iraq [4]. In 2009, $20,000$ confirmed cases of TBI occurred amongst deployed personnel [5]. TBI is classified as mild, moderate or severe based on the level of consciousness and a variety of factors including motor and verbal responses after resuscitation [1]. For patients with severe TBI, the mortality is between $30\% - 50\%$ and 90% of these patients die within 48 hours of injury due to excessive intracranial pressure and brain stem herniation [3].

In most cases of mild and moderate TBI, the effects of secondary injury are worse than the effects of primary injury (initial impact) and occur on a much longer time scale [1, 2, 4, 6]. Primary injury triggers multiple, interacting and independent cascades of biological reactions in the brain tissue that result in secondary injury. In particular, irregular intracellular calcium homeostasis is a critical factor in white and grey matter secondary injuries [1]. External forces are translated into irregular calcium homeostasis in the brain and result in the deterioration of white matter via multiple actions. For example, influx of calcium ions in mitochondria can lead to programmed cell death [7]. Many psychiatric illnesses have also been linked with TBI. For example, military personnel patients diagnosed with mild TBI have reported depression, post traumatic stress

disorder (PTSD), insomnia and suicidal symptoms [10, 4, 6]. Moreover, military personnel who have sustained more incidents of TBIs have reported more severe psychological symptoms and are at a greater suicide risk [8]. Unfortunately, almost all attempts to create drugs to treat the effects of secondary injury have resulted in failed drug trials due to a lack of understanding of the kinetics of the progressive and delayed degenerative process [11, 4]. There is some consensus about the series of events that occur after the influx of calcium (and other) ions but a detailed understanding is lacking. Additionally, a big question in this field is which mechanosensory transduction molecules are involved in translating external forces to an ion imbalance and the exact mechanisms involved.

Cellular and sub-cellular components across varying length scales susceptible to different stretch and shear thresholds could physically be disrupted by blast induced pressure waves and the resulting high accelerations. For example, at sub cellular scales, overstretch within axonal cytoskeletal microtubule networks or synaptic densities could occur. At a larger, cellular, scale overstretch could occur at bundled projection axons that connect large central nervous system features, such as within cerebellar peduncles connecting the cerebellum to the brainstem [12]. Moreover, disruptions in axonal connections can alter synaptic signal transfer and communication and may also trigger delayed cell death programs (apoptosis) [13]. Sarntinoranont et al. [12] subjected rat brain tissue slices to a high intensity pressure wave and observed the subsequent neuronal injury to be significantly greater than injury associated with creating the tissue slices. Figure 1.1 shows the experimental apparatus and the pressure profile the rat brain tissue slices were subjected to in the study. Figure 1.2 shows time series images of the rat brain tissue slices captured during the experiment as

the pressure wave traverses the tissue and the surrounding medium. Tissue is extensively deformed as a result of the pressure wave. Tissue damage also occurs as a result of cavitation, which is believed to occur due to negative pressures. The gas bubbles nucleated after 3.5 msec, grew over a period of 0.6msec, and collapsed at 4.8 msec. Previously, cavitation bubbles from the transmission of shock waves under controlled conditions have been show to cause localized vessel and cell injuries [14, 15, 16]. Nonetheless, central nervous system damage due to cavitation effects is not well established mainly as a result of the difficulty associated with detecting transient bubble formation and collapse within the skull and brain [12].

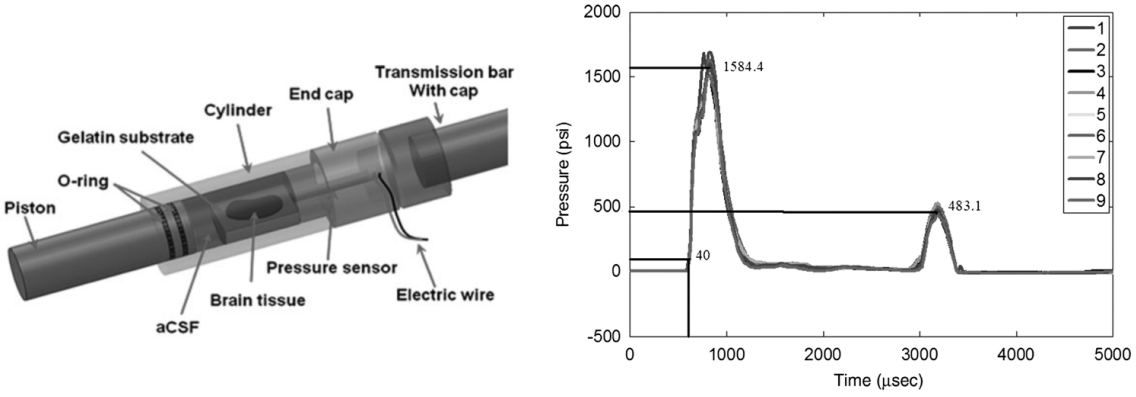

Figure 1.1: Experimental apparatus and pressure profile in study conducted by Sarntinoranont et al. *Left:* The rat brain tissue slice was placed in the cylindrical specimen holder filled with gelatin and artificial cerebrospinal fluid (aCSF). The pressure wave was introduced into the aCSF chamber by a sliding piston. The piston did not impact the tissue slice or gelatin substrate directly and the momentum was transferred to the tissue slice and gelatin via the surrounding fluid. *Right:* Artificial cerebrospinal fluid (aCSF) pressure profile during the experiment. The second peak pressure wave was a reflected wave. Figure modified from [12].

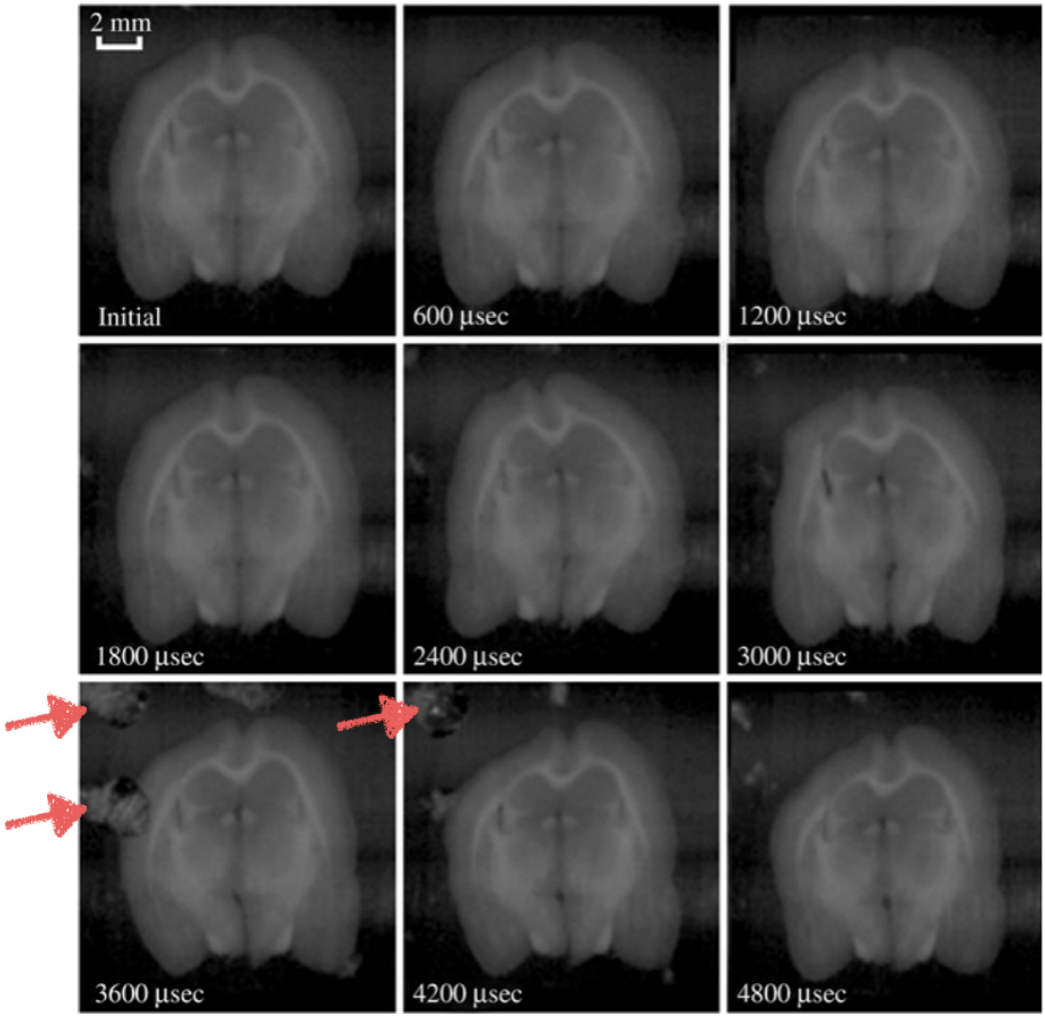

Figure 1.2: Time series of images captured during study conducted by Sarntinoranont et al. Extensive tissue deformation and cavitation occurs as pressure wave traverses the tissue and surrounding medium. Large gas bubbles (indicated by red arrows) nucleated after 3.5 msec, grew over a period of 0.6msec, and collapsed at 4.8 msec. Figure modified from [12].

Cells sense and respond to externally applied forces on many different time scales [19, 20, 21, 22, 23]. Changes such as channel activation can be observed on a scale of seconds, but others such as gene expression, protein synthesis and morphological changes can last for hours [24]. The detailed knowledge of how mechanical forces are converted into chemical signals is still emerging. These include the force-induced exposure of cryptic peptide sequences, the opening of mechanosensitive ion channels as well as strain dependent receptor-ligand interactions [38]. For example, Margadant et al., showed that force dependent stretching of the talin1 protein revealed vinculin binding sites *in vivo*, where the talin1-vinculin complex eventually led to the modification of cytoskeleton. In this way, the sensor acted to harden or soften the cell in different mechanical environments [39]. In another example Weisner et al. [17] developed a mathematical model that describes the recognition and transduction of shear stress to cytosolic-free calcium in endothelial cells. Exogenous calcium is presumed to enter the cell via shear stress gated ion channels and increasing shear stress (above a threshold) increases the cytosolic-free calcium concentration. Figure 1.3 shows the cytosolic-free calcium calcium concentration at different fluid shear stress levels with (bottom) and without (top) an agonist in the perfusate. In a study conducted with single glial cells, Charles et al. [18] mechanically stimulated single glial cells by a micropipette and observed a spike in intracellular calcium concentration and subsequent oscillations. The calcium wave was communicated to neighboring glial cells and similar spikes and oscillations were observed in these cells as well (Figures 1.4 and 1.5). The amount of force applied to glial cells in this study was not well defined [13].

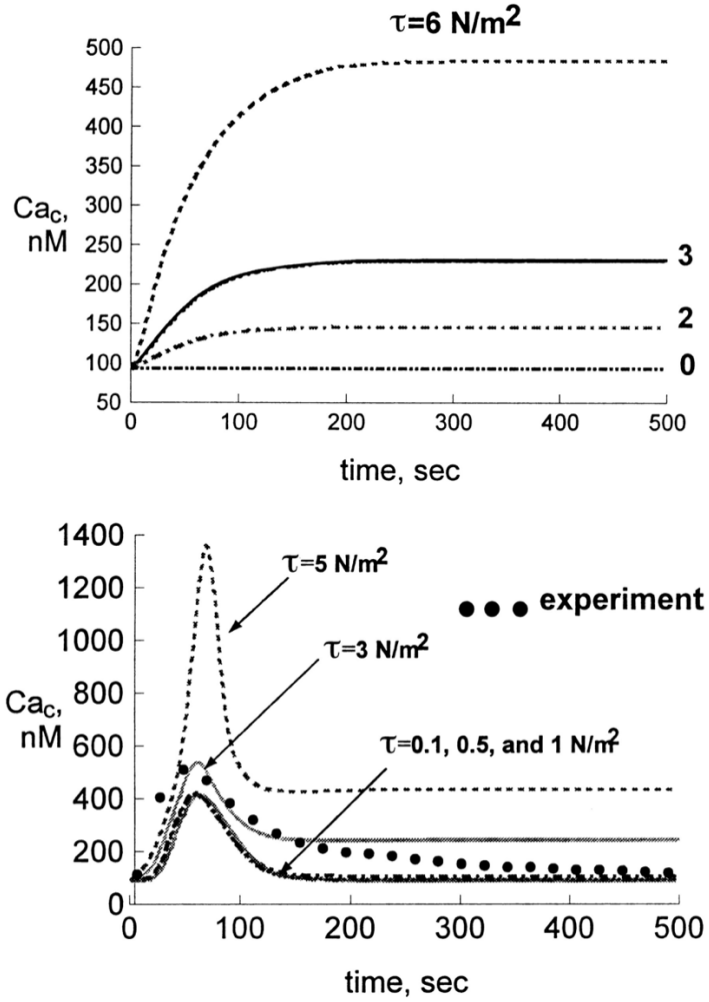

Figure 1.3: Results of model created by Wiesner et al. The mathematical model describes the cytosolic-free calcium response in endothelial cells to fluid shear stress. *Top:* Cytosolic-free calcium concentration at different shear stress levels. The perfusate is agonist free. The plateau level increases with increasing shear stress. The plots, based on calculations, are in agreement with experiments. *Bottom:* Cytosolic-free calcium concentrations at different shear stress levels. In this case, an agonist is present in the perfusate. Below $\tau = 1N/m^2$, shear stress exerts a relatively small influence upon the cytosolic-free calcium concentration. This influence in exerted through modulation of mass transfer of agonist. Above $\tau = 1N/m^2$, cytosolic-free calcium concentration (plateau and peak) increases as shear stress increases. The transient peak is due to agonist stimulated release from intracellular stores and the sustained plateau is attributed to the influx of extraracellular calcium. Figures modified from [17].

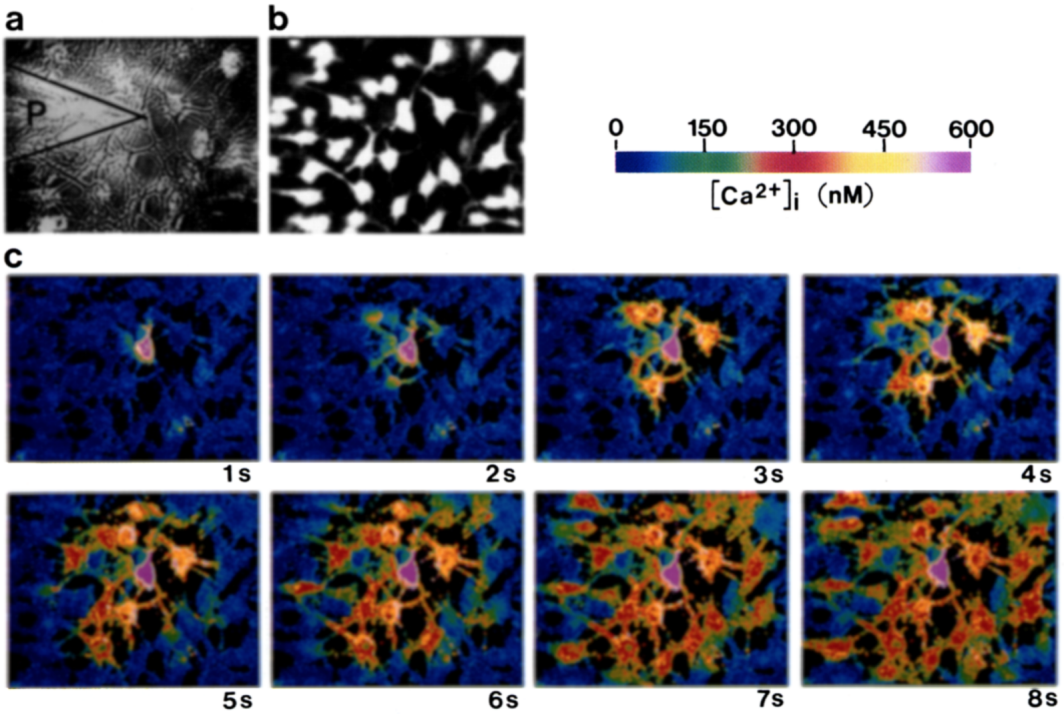

Figure 1.4: Results of study conducted by Charles et al. showing increase in intracellular calcium levels in small population of glial cells. **(A)** A micropipette (P) is positioned over a single cell and is used to mechanically stimulate the cell. **(B)** A fluorescence image showing individual cells. **(C)** Snapshots showing intracellular calcium levels in cells after an individual cell is mechanically stimulated. The wave of calcium signaling is communicated to neighboring cells by the stimulated cell. The scale of all images in $155\mu m$ vertically by $210\mu m$ horizontally. Figure modified from [18].

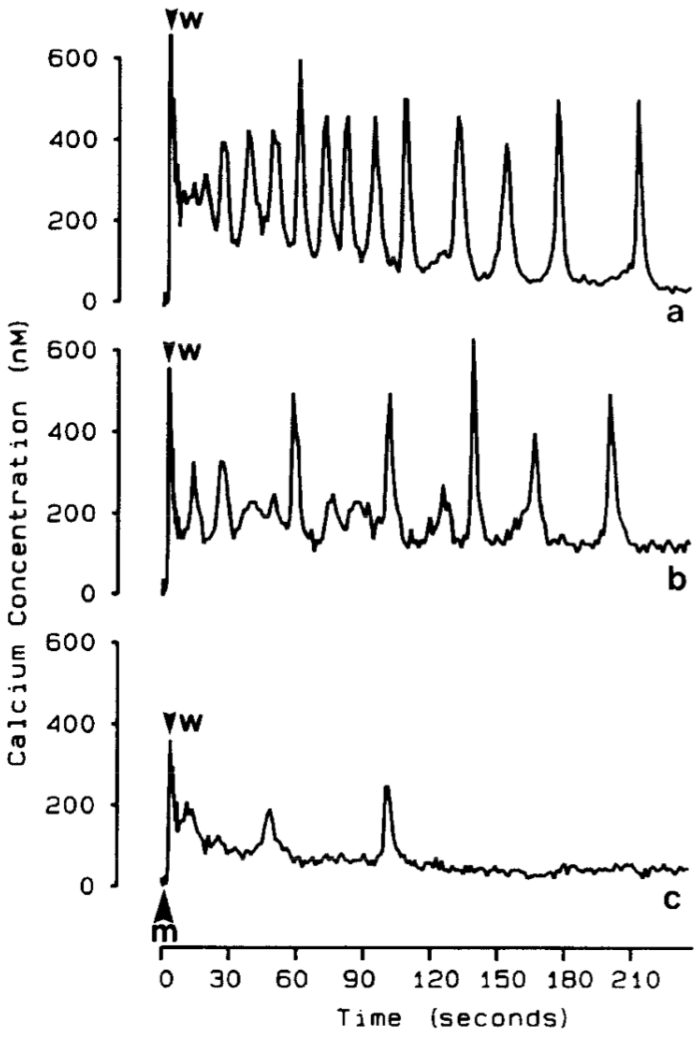

Figure 1.5: Results of study conducted by Charles et al. showing oscillations of intracellular calcium levels induced by mechanical stimulation. Mechanical stimulation was applied at time 0, as indicated by label ″m″. The communicated calcium wave is indicated in each tracing by the label ″w″. None of the plots represent the stimulated cell. *Top:* The most commonly observed pattern. The period of oscillation and the baseline decrease over time. *Middle:* A less commonly observed pattern of oscillation. The period of oscillation and the baseline remain relatively constant over time. *Bottom:* An example where only a few oscillations were observed. Figure modified from [18].

How cells react to forces is not well known and the focus for the field of traumatic brain injury has been on the identification of transduction channels that are directly gated by mechanical force [40]. The three classes of channel proteins that are being considered to be the mechanosensory transduction molecules in animals are: DeG/ENaC (degenerin)/epithelial Na+ channel) subunits, transient receptor potential (TRP) proteins and two-pore-domain K+ channel subunits. There is uncertainty regarding the specific function of all three types of channels. Moreover, there has been evidence that the first two of these protein channels are involved in transduction of mechanical signals in some organisms [44, 45, 46] but their role in other organisms, especially in mammals is uncertain [40]. There is also uncertainty about the mechanisms through which these channels open and three mechanisms have been proposed. In the membrane force model the channel opens when the membrane is stretched and closes when the membrane relaxes (Figure 1.6) [42]. In the dual-tether model (Figure 1.7), the membrane opens not as a result of forces in the membrane but through direct linkage to extracellular components (similar to a trap door) and in the single-tether model the channel opens via a combination of both mechanisms [40].

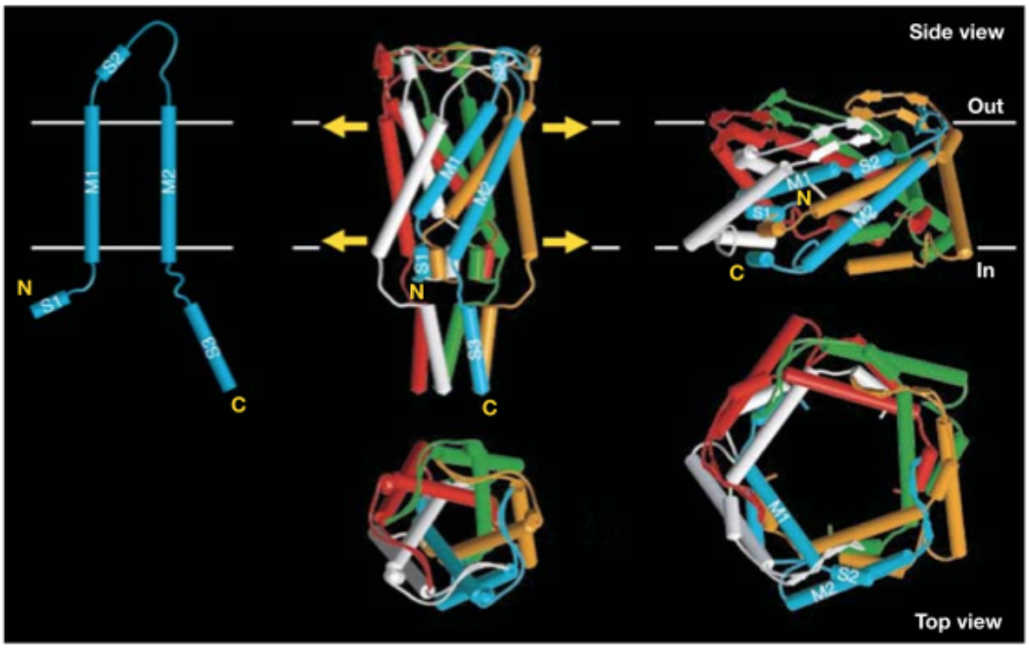

Figure 1.6: Membrane force model. Only the forces in the membrane and no other proteins are required to gate some bacterial channels, such as the mechanosensitive channel of large conductance (MscL) in E. coli. As the bacterium swells, the forces in the membrane rearrange the channel from a closed to an open configuration. *Top Left:* Helical segments (S1, S2, S3) and transmembrane helices (M1, M2) in one MscL subunit. *Middle:* Closed-resting confirmation. *Right:* Open confirmation. The opening is about 30Å in diameter. Horizontal lines show approximate positions of the inner and outer boundaries of the membrane. Figure modified from [41].

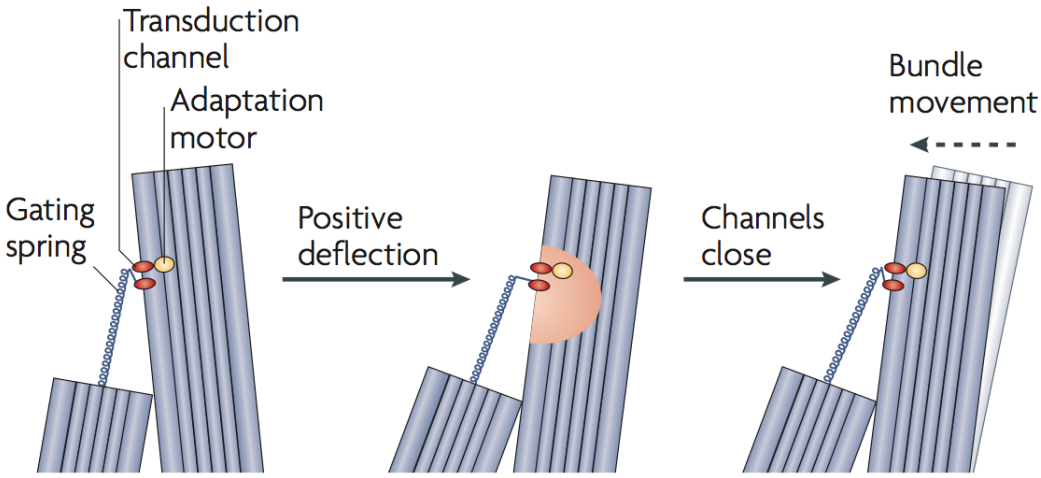

Figure 1.7: Dual Tether Model. Transduction and fast adaptation in stereocilia. Positive deflection opens the channel, allowing calcium ions to enter the cell (pink shading). Bundle movement in the opposite direction leads to channel closure. Forces in the membrane are not needed to open the channel. Figure modified from [43].

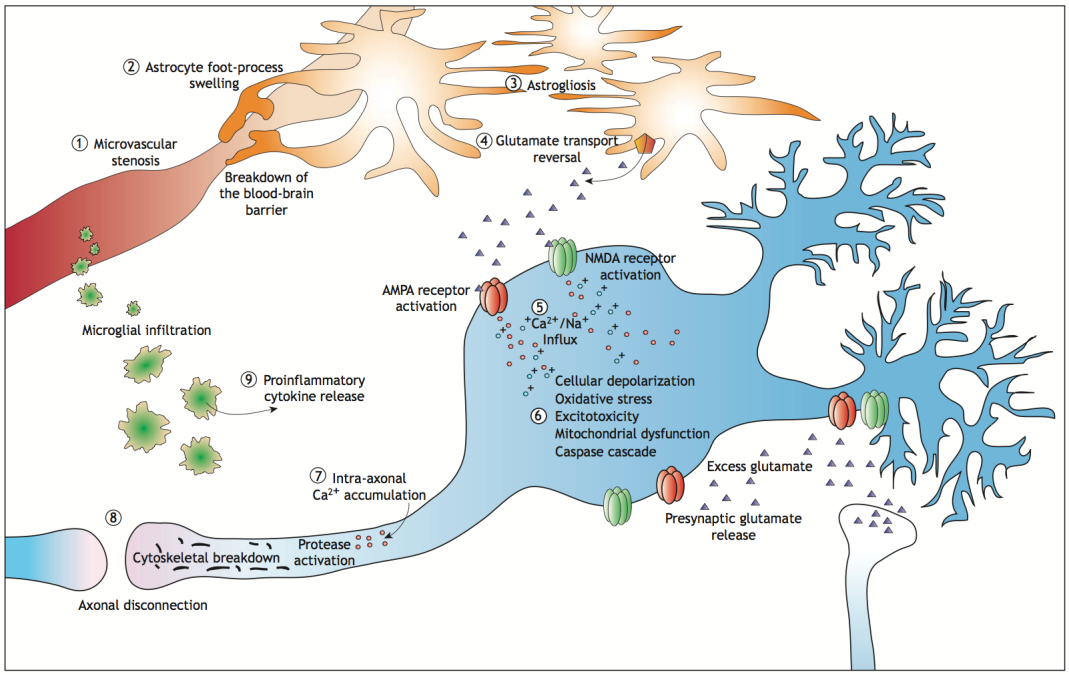

Figure 1.8: Some major pathways associated with the progression of secondary injury after TBI. Figure is modified from [1].

Secondary injuries following TBI, are multiple, parallel, interacting and interdependent cascades of biological reactions (Figure 1.8 shows some major pathways associated with secondary injury). The opening of mechanosensitive channels leads to the influx of calcium (and other) ions in the cell in the time scale of seconds [53]. Abnormal calcium homeostasis in the brain is critical to the progression of grey and white matter secondary injury and leads to multiple reaction pathways at multiple time scales [1]. Increased calcium ions in the axon (white matter) leads to activation of enzymes that degrade key structural proteins that destroy proteins responsible for the maintenance of shape and transport in axons, ultimately leading to axon swelling and disconnection of the two parts of the swollen axon, which can take from 12 to 24 hours after the influx of ions [47]. Increased calcium ions in the neuronal cell body (grey matter) leads to excitotoxic cell death, initiation of programmed cell death and post-synaptic receptor modifications. Inside the cell, the excessive uptake of calcium ions by the mitochondria (which maintains homeostasis of calcium and other ions, and produces ATP) causes membrane depolarization, the opening of membrane permeability transition pores and the release of initiation factors of programmed cell death [48]. As a result, the mitochondria can no longer function and this further leads to the influx of calcium ions (and other ions) due to loss of calcium buffering capacity and the bioenergetic failure of ATP-dependent ion pumps due to lack of ATP. There is also significant cross talk between the different pathways. For example, the reaction of superoxide (derived from mitochondria) with nitric acid (derived from a receptor in the excitotoxic pathway) creates the highly reactive nitrating species peroxynitrite which leads to fatal cellular process such as DNA fragmentation [1, 49]. In addition to the damage caused to neurons by the uptake of calcium ions, other reaction pathways are

also initiated including the destruction of microvasculature that could lead to the breakdown of the blood-brain barrier and excessive build up of glutamate which could lead to epileptic activity.

As the deterioration of grey and white matter is a progressive process, many, if not all of the effects can be avoided if a better understanding of the kinetics of the process is achieved. The aim of this study was to develop computational tools to estimate extracellular and sub-cellular forces in a single cell (or a small population of cells) when it is subjected to external forces such as due to blast waves traversing through tissue and the subsequent formation and rupture of cavitation bubbles. To this effect the ability to capture the shape (or geometry) of cells and nuclei of regular-shaped cells (e.g. HL60 cells) and irregular-shaped cells (e.g. astrocytes) from images was developed. The resulting geometries of the cytoplasm and the nucleus can be meshed with different meshing characteristics (different number of mesh points), which is used to create a viscoelastic model of a cell. To create the viscoelastic model, the edges connecting the mesh point can be replaced with Voigt elements. An open source software package was developed, which automatically generates a system of coupled ODEs with inequality constraints describing the kinematic response of the viscoelastic model to an external force. In order to create an accurate viscoelastic model of a cell, the Voigt parameters need to be estimated from experimental data. An optimization procedure was created to develop the ability to estimate parameters from experimental data. These computational tools will aid in future studies to correlate forces at the cellular length scale with signaling data, such as intracellular calcium signaling, to develop a mechanically coupled signal transduction network for secondary injury following mild traumatic brain injury.

CHAPTER 2

BACKGROUND

2.1 Modeling Cells as a Viscoelastic Structure

Cells are enveloped in a membrane (lipid bilayer), filled with fluid (cytosol) and supported by a polymeric scaffold (cytoskeleton), which gives rise to the cells' viscoelastic properties [26, 28, 29, 30, 31]. Cells can be modeled using linear viscoelastic elements [27, 59] which consists of a Hookean spring (represents the relationship between stress and strain in a linear elastic material) and a Newtonian dashpot (represents viscous resistance and has a linear relationship between the force applied and the deformation rate). A Maxwell element and a Voigt element are two examples of linear viscoelastic material models. In a Voigt element, the spring and the dashpot are in parallel. When an external force is applied, the strain in both elements is always equal and the total stress is the sum of the stress in the spring and the dashpot. This results in the following governing equation for the Voigt element, where σ is the normal stress, ε is the normal strain , E is the Young's modulus or stiffness of the spring, η is the viscosity associated with the dashpot and $d\varepsilon/dt$ is the strain rate.

$$\sigma = E\varepsilon + \eta\frac{d\varepsilon}{dt} \tag{2.1}$$

In a Maxwell element, the spring and the dashpot are in series. When an external force is applied, the stress in both elements is always equal and the total strain is the sum of the strain in the spring and dashpot. This results in the following governing equation for the Maxwell element.

$$\frac{d\sigma}{dt} + \frac{E}{\eta}\sigma(t) = E\frac{d\varepsilon}{dt} \tag{2.2}$$

To understand the behavior of these two elements, a two-stage standard test can be performed. Initially, there is no stress or strain in the system. In the first stage (creep phase), a constant stress is applied and the time-dependent response of the strain is observed. In the second stage (stress relaxation phase), the system is fixed at its current strain (at t_1), and the time-dependent response of stress is observed. A Voigt element has a characteristic relaxation associated with it. It is defined as $T = \eta/E$ and is the time taken for deformation of the Voigt element to reach a proportion of $(1 - \frac{1}{e})$ of its final or maximum value [25]. Figure 2.1 shows the response of these elements in this test.

Jamali et al. utilized the Voigt model to build a two dimensional complex structure of a cell, which can be described as being viscoelastic [27]. This cellular model allows the cell shape to deform as external forces are applied and the forces can be calculated on points on the cell membrane (cellular length scale) or on points inside the cell (sub-cellular length scale). This framework can be used to model a cell which is mechanically coupled to the extracellular matrix, is easily extensible to model a three dimensional cell and can incorporate biochemical signaling. Figure 2.2 shows a schematic of the cellular model the researchers build using the Voigt elements. The cell is represented as a circular structure. The cell and nuclear membrane is discretized arbitrarily into N_0 nodes (points), where each node on the cell and nuclear membrane represents $1/N_0$ of the mass of the cytoskeleton and nucleus, respectively. Neighboring nodes in each membrane are connected by Voigt elements. To model the cytoskeleton, each node in the cell membrane is connected to a node in the nuclear membrane

with a Voigt element. Additionally, to represent the nuclear cytoskeleton, each node on the nuclear membrane is connected to two other nodes in the nuclear membrane with Voigt elements. There are three parameters associated with a Voigt element: the rest length of the spring, the spring constant and the viscosity parameter of the dashpot. Jamali et al. used values obtained from experimental studies to model cells. Initially, the parameters were uniform throughout the cell but were later changed to simulate complex cell behavior such as motility and mitosis. By manipulating the three parameters, the shape, stiffness and viscoelastic behavior of the cell can be controlled. More importantly, because of the use of Voigt elements, different parts of the cell can have different viscoelastic properties. The inclusion of the nucleus in the model is important for cellular mechanotransduction, as the forces that are experienced by the nucleus can lead to events such as gene expression [37].

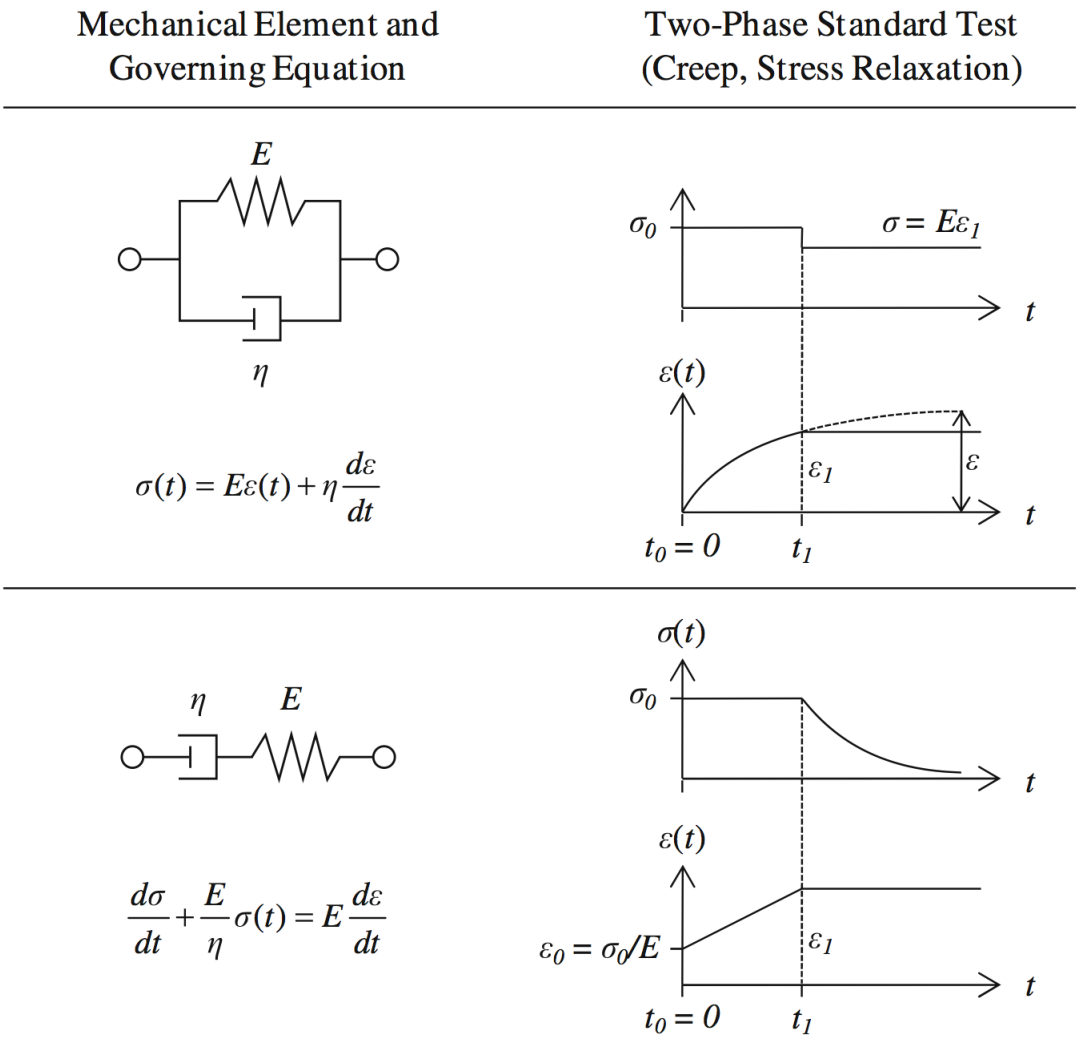

Figure 2.1: The Voigt (spring and dashpot in parallel) and Maxwell (spring and dashpot in series) elements are simple viscoelastic material models. The creep and stress relaxation phases of the standard two-phase test are shown. In the first stage (creep phase), a constant stress in applied and the time-dependent response of the strain is observed. In the second stage (stress relaxation phase), the system is fixed at its current strain (at t_1), and the time-dependent response of stress in observed. Figure modified from [26].

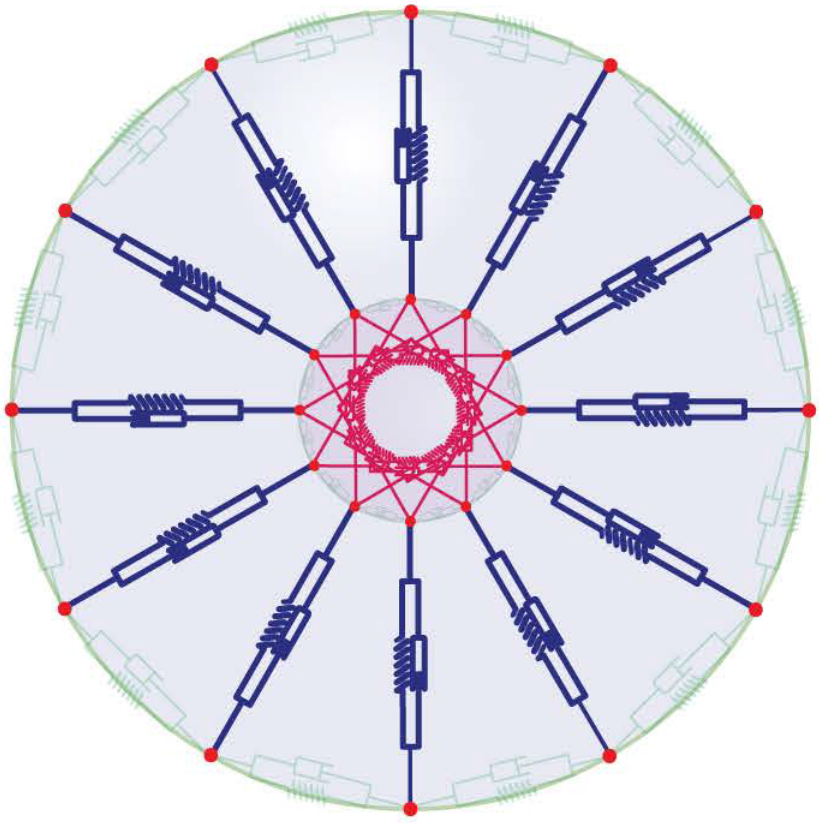

Figure 2.2: A viscoelastic mechanical model of a cell as created by Jamali et al. The red nodes have mass and the sum of the mass of nodes is equal to the mass of the cell. The nodes on cell membrane are connected with adjacent nodes by Voigt elements (green) and model the cell membrane. Similarly, the neighboring nodes on the nuclear membrane are connected with Voigt elements (green). The cytoskeleton is modeled by connecting nodes on the nuclear membrane with nodes on the cell membrane with Voigt elements (blue). The nuclear cytoskeleton is modeled by connecting nodes on the nuclear membrane with Voigt elements (red). Figure modified from [27].

CHAPTER 3

METHODS

3.1 Capturing and Meshing Cellular and Nuclear Shapes

Persson and Strang [55, 56] developed an algorithm that allows for the rapid generation of meshes of arbitrary 2D areas and 3D volumes. This algorithm and software (written in Matlab) can be used to mesh images of cells into discrete nodes. The input for this software is a *Signed Distance Function* for the geometry, which gives the shortest distance from any point in space to the boundary of the domain. The sign is negative inside the region and positive outside. For example, a unit circle in 2D has a *Signed Distance Function* $d = r - 1$, where r is the distance from the origin. For more complicated geometries with irregular shapes, for example a cell, the distance function can also be computed by interpolation between values on a grid.

The iterative algorithm consists of two main steps (Figure 3.1). Initially, a uniform distribution of nodes corresponding to equilateral triangles within the geometry is created. In the first step, the mesh points are modeled as nodes of a truss and the edges connecting the nodes of the triangles are modeled as truss structures. All the nodes exert a repulsive force on the other nodes to which they are connected. In addition, nodes on the boundary of the geometry are subjected to a force perpendicular to the boundary to keep them inside. In this first step, the equations describing the motion of the mesh points as a result of the forces exerted on them are solved. In the second step of the algorithm, the topology is adjusted by the Delaunay triangulation algorithm. In the Delaunay algorithm, the mesh point positions are adjusted so that non-overlapping tri-

angles fill the positions of the geometry, such that every edge is shared by, at most, two triangles and the circumference of every triangle contains no other mesh point. The steps are repeated until a stable meshing of the geometry is achieved. The user specifies the *element size function* $h(x, y)$, which corresponds to the relative edge length of the mesh triangles. The *element size function* can be a fixed value, which results in a uniform mesh, or it can be a function of the geometry, which results in a non-uniform mesh (Figure 3.2). The number of nodes in the mesh is implicitly controlled by the *element size function*. The output from the program are the node positions (an $N - by - 2$ array containing the x, y coordinates for each of the N nodes) and the triangle indices (a row associated with each triangle has 3 integer entries to specify node numbers in that triangle).

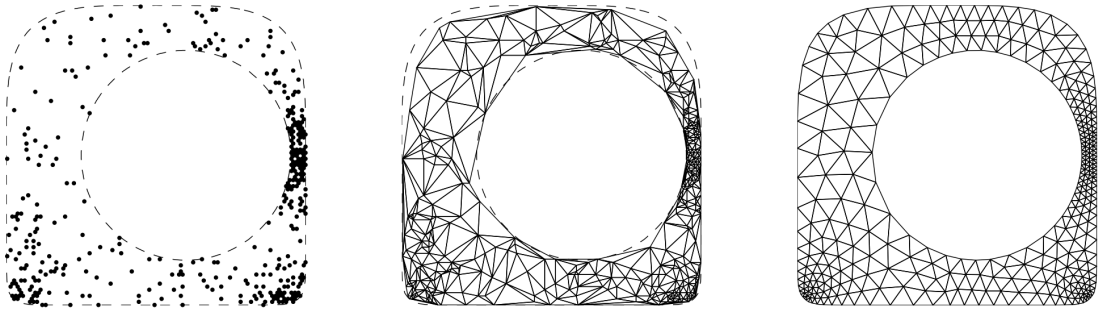

Figure 3.1: The steps involved in the meshing algorithm developed by Persson and Strang [55, 56] . Initially, a uniform distribution of nodes corresponding to equilateral triangles within the geometry is created. In the first step of the iterative algorithm, the mesh points are modeled as nodes of a truss and the edges of the triangles are modeled as trusses. The force equations are solved for equilibrium. In the second step of the algorithm, the topology is adjusted by the Delaunay triangulation algorithm. In this example the resulting meshed geometry has non-uniform meshing. Figure modified from [56].

For complex geometries a closed form expression for the *Signed Distance Function* cannot be evaluated and a discretized representation of the geometry

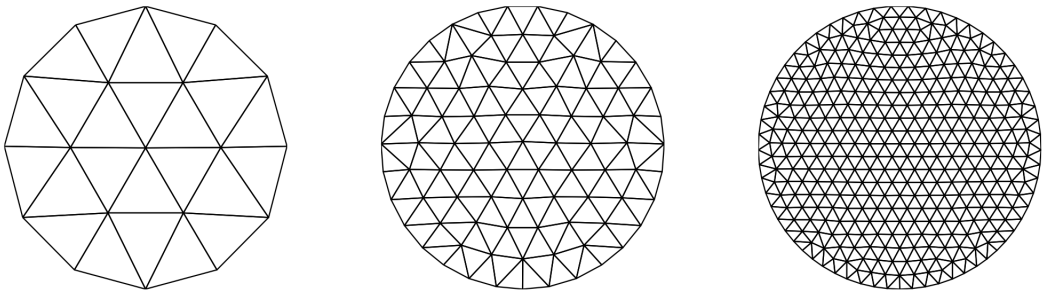

Figure 3.2: A circular geometry uniformly meshed using different *element size functions* $h(x, y)$, which corresponds to the relative edge length of the mesh triangles. The *element size function* implicitly controls the number of nodes in the resulting mesh. Figure modified from [56].

can be inputted into the software instead. In this discretized representation, the function values (distance to closest boundary) for a finite set of points is stored and interpolation is used to approximate the function for arbitrary points. Chan and Vese [61] developed a very effective model where edges can be easily detected from images, and a discretized signed distance function can be calculated. This model is based on Mumford-Shah segmentation techniques [62] and the level set method. In this model, an initial curve is evolved which divides the image into two segments. The curve is then allowed to move in the region until it detects desired boundary. This model is not based on an edge-function (the gradient of the image) to stop the evolving curve on the desired boundary but instead uses the relative intensities of the segments. This offers the advantage that edges can even be detected if the image is noisy and the edge is not well defined (Figure 3.3).

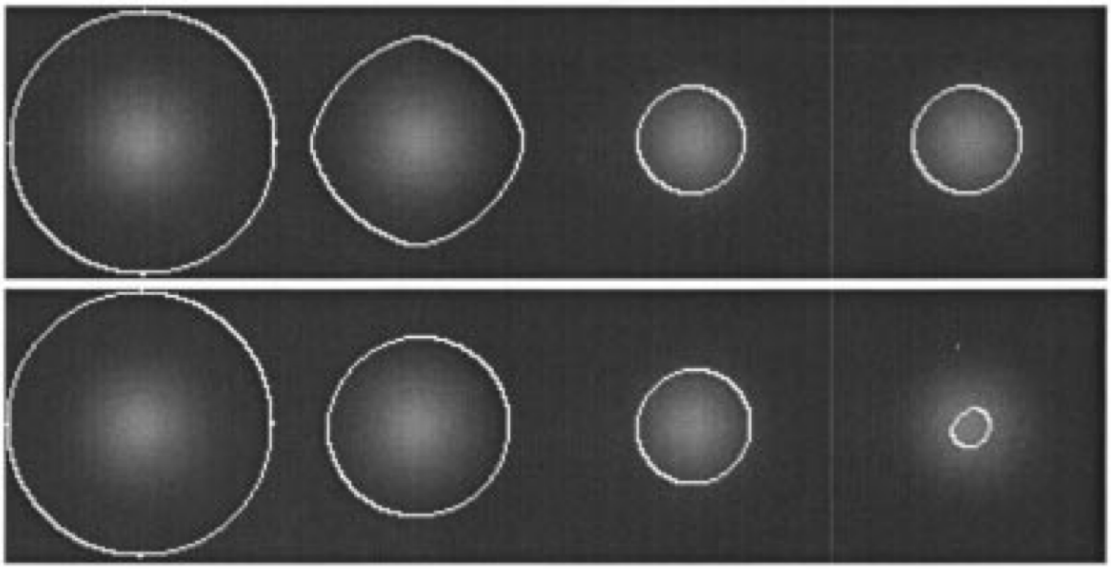

Figure 3.3: *Top:* An object without a well defined boundary is detected using the algorithm developed by Chan and Vese without edge function. *Bottom:* The object is not detected using a classical model with edge-function. Figure modified from [61].

3.2 A System of ODEs with Inequality Constraints

When a geometry has been meshed, the edges connecting the mesh points can be modeled as Voigt elements and a system of ODEs can be developed after taking the force balance around each node in each coordinate direction. Equations 3.1 and 3.2 describe the dimensionless equations in coordinate direction m for node (i, j) that is connected to node (k, l) by a Voigt element. In the following equations k (units: $\left[1/t^2\right]$) denotes the element spring constant and μ (units: $[1/t]$) denotes the dampening coefficient, $\Theta_{k,l\to i,j} \equiv \mu^2/k$ is the dimensionless derived Voigt parameter, $\tau \equiv kt/\mu$ is the dimensionless time, $\hat{x}^m_{i,j} \equiv x^m_{i,j}/L_m$ is the dimensionless coordinate in direction m where L_m is the characteristic length in coordinate direction m, $\hat{v}^m_{i,j} \equiv \mu v^m_{i,j}/(kL_m)$ is the dimensionless velocity in coordinate direction m, $\hat{F}^m_{i,j} \equiv \mu^2 F^m_{i,j}/(k^2 L_m)$ is the dimensionless external (applied) force in coordinated direction m, $\hat{l} \equiv l/(L_1 L_2 \dots L_N)^{(1/N)} \equiv l/(L_1 L_2)^{(1/2)}$ is the dimensionless spring length in N and 2 dimensions, respectively. The quantity $\alpha_{k,l\to i,j} = \left(d\left(\mathbb{P}_{k,l}, \mathbb{P}_{i,j}\right) - l\right)/d\left(\mathbb{P}_{k,l}, \mathbb{P}_{i,j}\right)$, denotes a dimensionless fractional extension/contraction length, where $d\left(\mathbb{P}_{k,l}, \mathbb{P}_{i,j}\right)$ denotes the distance operator between nodes $\mathbb{P}_{i,j}$ and $\mathbb{P}_{k,l}$.

$$\frac{d\hat{v}^m_{i,j}}{d\tau} = \Theta_{k,l\to i,j}\Big(\hat{\alpha}_{k,l\to i,j}(\hat{x}^m_{k,l} - \hat{x}^m_{i,j}) + (\hat{v}^m_{k,l} - \hat{v}^m_{i,j})\Big) + \hat{F}^m_{i,j} \tag{3.1}$$

$$\frac{d\hat{x}^m_{i,j}}{d\tau} = \hat{v}^m_{i,j} \tag{3.2}$$

$$\xi_{k,l\to i,j} \leqslant d\left(\mathbb{P}_{k,l}, \mathbb{P}_{i,j}\right) \leqslant \zeta_{k,l\to i,j}, \qquad \forall_{k,l\to i,j} \tag{3.3}$$

In some cases, when the forces on the nodes are large, a node can cross over other nodes (the area can flip over itself). Moreover, forces can become localized over a few nodes and not spread to the whole area, leading to unrealistic results

(Figure 3.4a). Provot [57] addressed a similar problem when trying to animate a cloth object, modeled as a network of masses and springs. In Figure 3.4, gravity is acting on all the node points and the top left and top right nodes are fixed. To achieve realistic results, the effect of increasing the stiffness of the springs under certain conditions was considered, but this lead to very stiff equations. Eventually constraints were implemented on the springs connecting the nodes to achieve a stable solution. After each iteration of the ODEs, if the length of the springs connecting two nodes was greater than a certain distance, the positions of the nodes connecting the springs were modified (on the same axis), to reduce the distance of the spring to the desired distance. This lead to a stable and more realistic solution as the forces were spread out over the cloth object.

A similar technique was implemented in this study to solve the system of first order ODEs with inequality constraints. However, in addition to enforcing a maximum constraint on the nodes connected with Voigt elements, a minimum constraint was also enforced. A Modified Euler algorithm, a second order method, was used to solve the system of equations, as is consistent with previous studies [57, 58]. The modified Euler algorithm was preferred over built-in solvers in MATLAB (e.g. ode45), as a check can be performed after every time step to determine if the constraints are met and the positions of the nodes which do not satisfy the constraints can be corrected. The nodes are moved an equal amount either towards each other or away from each other to meet the constraint. If one of the nodes is fixed in place, only the other non-fixed node is moved. The nodes are always moved along the axis that connected them initially. When the nodes for an edge were corrected, this sometimes led to the neighboring edges failing the constraint. To account for this, the constraints were checked and corrected multiple times before the next time step. Equation

3.3 describes the constraints on the distance between nodes $\mathbb{P}_{i,j}$ and $\mathbb{P}_{k,l}$. $\xi_{k,l\to i,j}$ is the minimum distance and $\zeta_{k,l\to i,j}$ is the maximum distance between the nodes. The complexity of the constraints in $O(n^2)$, where n is the number of nodes in the model.

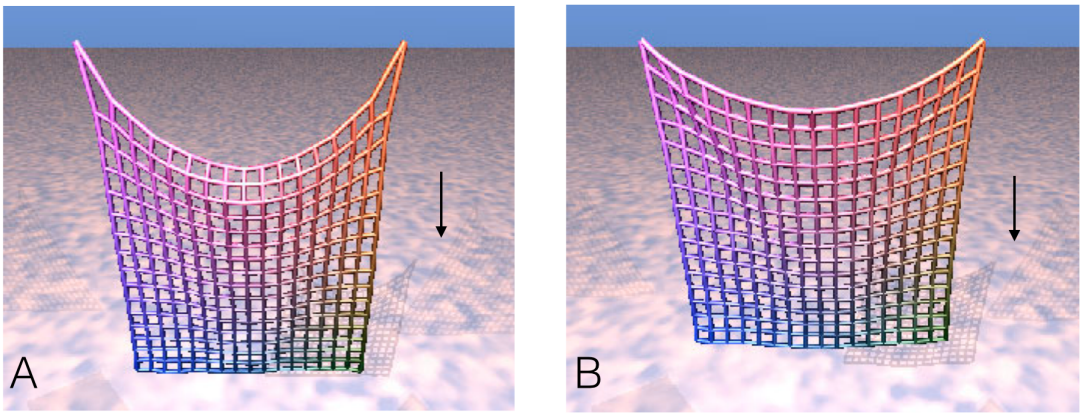

Figure 3.4: Elastic model of a cloth object hanging by two adjacent corners. The cloth object is modeled as a network of masses connected with springs. The top left and the top right nodes are fixed and gravity is acting downwards on all the masses. **(A)** No constraints are applied. The forces are concentrated in a local area and the springs near the two fixed points are elongated the most. **(B)** Constraints are applied on the spring length. Forces are spread out over the whole object and lead to a more realistic result. After each iteration, whenever the distance between two nodes connected by a spring increases more than a specified amount, the node positions are modified to decrease the distance. Figure modified from [57].

3.3 Friedlander Waveform: Modeling Blast Forces

Blast waves from explosive devices are very similar to shock waves [64]. Figure 3.5 shows the typical pressure profiles for both shock waves and blast waves. Both waves have positive pressure components (compressive stress) followed by temporary negative components (tensile stress). The peak pressure is the highest and the lowest pressure. The rise time is a measure of how rapidly pressure changes from the ambient level to the maximum positive value and the pulse width is the amount of time pressure remains above a specified level. A classical free-field blast wave at a fixed location can be modeled by the Friedlander waveform (Equation 3.4) [63], where p^* is the highest peak pressure, t_d is the positive phase duration and b is the decay constant (Figure 3.6).

$$p(t) = p^* \left(1 - \frac{t}{t_d}\right) e^{-bt/t_d} \tag{3.4}$$

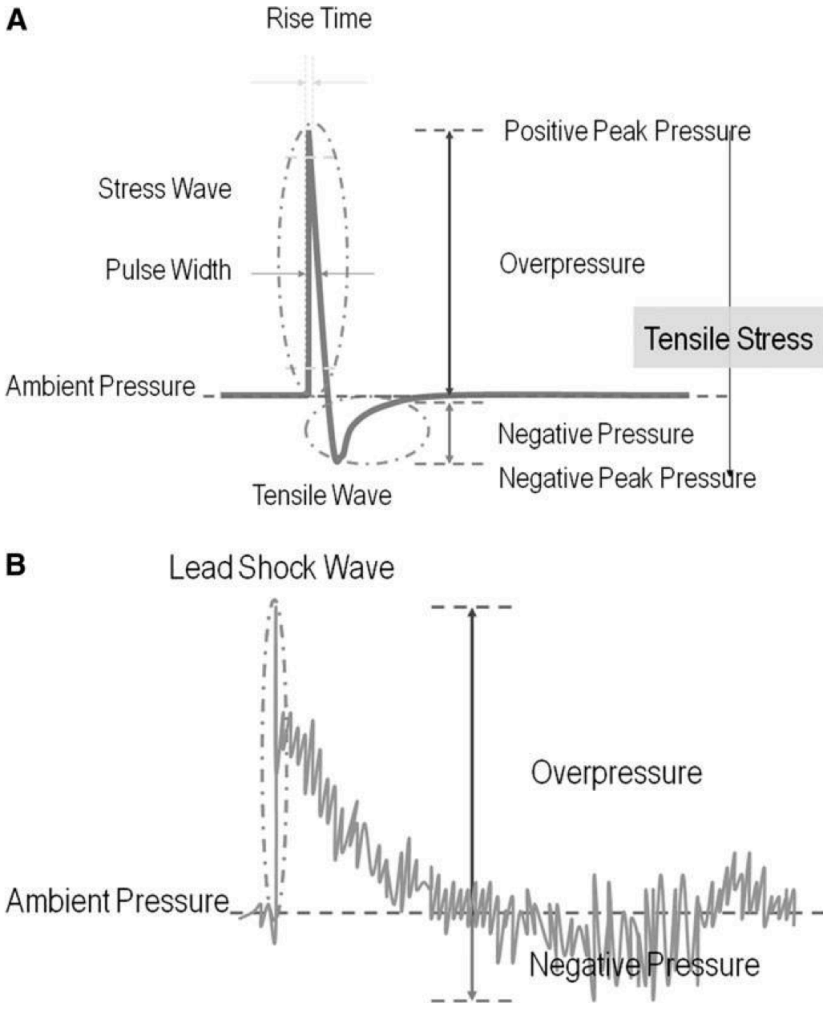

Figure 3.5: Pressure profiles of **(A)** a shockwave and **(B)** a blast wave. Both waves have positive pressure components (compressive stress) followed by temporary negative components (tensile stress). Figure from [64].

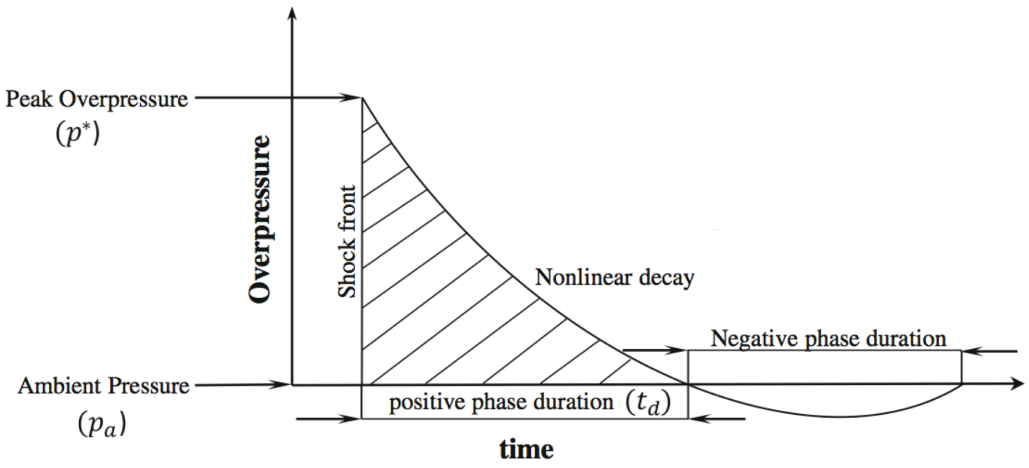

Figure 3.6: Mathematical representation of the Friedlander waveform, which can be used to model shock waves. Figure from [63].

3.4 Developing an Accurate Model Using Optimization Techniques

$$\min_{\Theta} \sum_{t \in t^{opt}} \sum_{i \in p^{opt}} \|\mathbb{P}_i^{real,t} - \mathbb{P}_i^{opt,t}\| \tag{3.5}$$

When external forces are applied to a group of cells in an experimental setup, high-resolution images of the deformation of the cells can be captured at multiple time steps. These images can be used to estimate the Voigt parameters of a viscoelastic cell model using an optimization technique. The optimization procedure can be developed without experimental data, using synthetic data. A Friedlander force can be applied to a viscoelastic model of a cell using a set of Voigt parameters and the positions of the nodes can be recorded at each time step as the system of equations governing the nodes is solved. This is the synthetic data. For the optimization procedure, optimization data can be created by using a randomly selected set of Voigt parameters and by solving the system of equations governing the nodes when the same external forces is applied. An objective function can be calculated using Equation 3.5, using selected nodes at a limited number of time steps (the sampling frequency). This time step should be larger than the time step at which the system of equations is solved using the modified Euler algorithm as the sampling frequency at which images can be taken in the experimental setup will be limited. Moreover, the temporal positions of some, but not all, nodes of the viscoelastic model can be estimated from the experiment. In Equation 3.5, $\mathbb{P}$ is the distance of a node from the origin, p^{opt} is the set of nodes that are being considered in the objective function and t^{opt} is the set of times that are being considered in the objective function (optimization time step). This objective function can be minimized over the set of Voigt pa-

rameters (Θ) using an optimization technique to solve for the set of parameters that were used to generate the synthetic data.

CHAPTER 4

RESULTS AND DISCUSSION

4.1 Capturing and Meshing Cellular and Nuclear Shapes

A mesh of an image of an HL60 cell was created. Figure 4.1(A) shows the image of the HL60 cell that was used and Figure 4.1(C) shows the graphical representation of the signed distance function for the cell that was created using the algorithm discussed in the previous section. To create the discretized signed distance function of the nucleus, only the red channel of the image was considered and the image was masked to hide the cell boundary so the shape of the nucleus could be effectively captured (Figure 4.2). The discretized signed distance function of the nucleus and the cell was meshed using the algorithm discussed in the previous section (Figure 4.3(A), (B)). Figure 4.3(C) shows the resulting meshed figure of the cell, which shows two distinct regions (the cytoplasm and the nucleus). This was created by first meshing the nucleus, and then meshing the cell around the nuclear mesh points. A uniform mesh was created for both the nucleus and the cell. Moreover, the same element size function (which controls the relative size of the edge length and the number of mesh points) was used for both the nucleus and the cytoplasm. The resulting mesh of the cell had 520 mesh points of which 198 were nuclear mesh points and 322 were cytoplasmic mesh points. The nodes on the nuclear membrane were

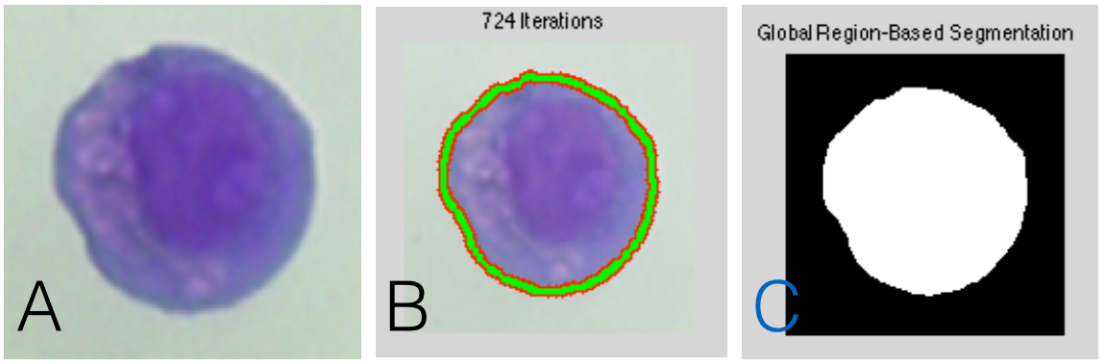

Figure 4.1: A discretized signed distance function is created from an **(A)** image of a HL60 cell. **(B)** The shape of the cell is captured effectively by the algorithm. **(C)** A graphical representation of the discretized signed distance function of the cell.

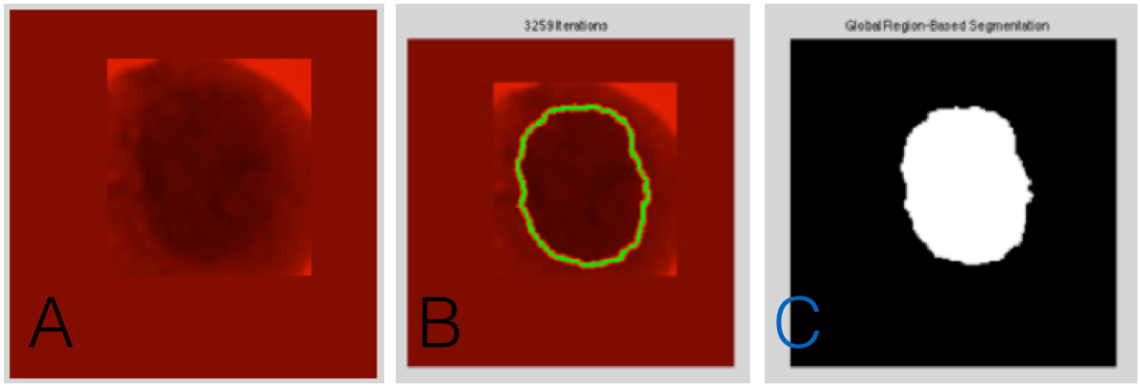

Figure 4.2: A discretized signed distance function of the nucleus is created from an **(A)** image of a HL60 cell. To effectively capture the shape of the nucleus, only the red channel is considered and the image is masked to hide the boundary of the cell. **(B)** The shape of the nucleus is captured effectively by the algorithm. **(C)** A graphical representation of the discretized signed distance function of the nucleus.

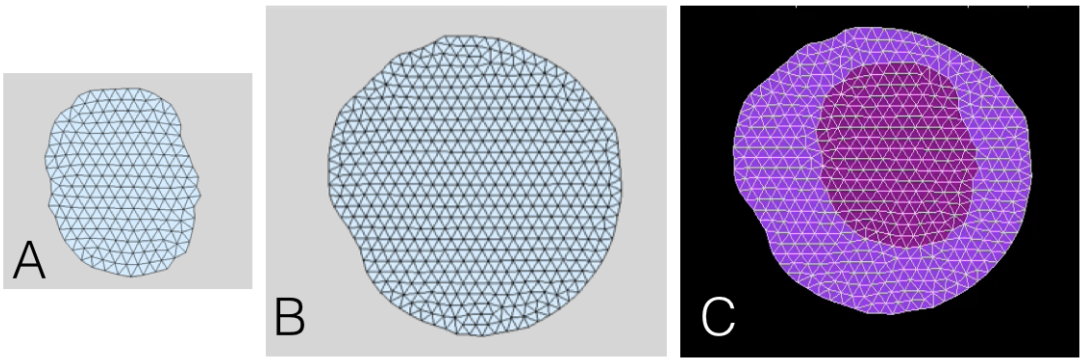

Figure 4.3: **(A)** Uniform meshing of the nucleus and **(B)** a uniform meshing of the cell. **(C)** The meshing of the whole cell shows two distinct regions of the cell. This was created by first meshing the nucleus, and then meshing the cell around the nuclear mesh points. The mesh of the cell has 520 mesh points of which 198 are nuclear mesh points and 322 are cytoplasmic mesh points. The same element size function (which controls the relative size of the edge length and the number of mesh points) was used for meshing the two regions.

4.2 Code Generator: Automatic Generation of a System of ODEs with Inequality Constraints

To automatically and rapidly generate model equations and other auxiliary code in several programming languages for any meshing geometry, an open-source software (Code Generator) was developed in Objective C language (Figure 4.4). The input for this program are two xml files, a geometry file and a transformation file (see Appendix A). The transformation file specifies which programming language the system of equation should be written in as well as other information, such as where the output should be saved. The geometry file contains a list of the coordinates of the mesh points, a list of the edges (pair of mesh points connected with a Voigt element) and the associated Voigt element parameters. This geometry file was created with another open-source software (Geometry File Generator), also developed in Objective C language. The input of the Geometry File Generator is the list of mesh point coordinates and the mesh point triangles that were generated with the meshing algorithm discussed in the previous section (see Appendix A). The resulting system of equations can be developed in multiple languages, but for this project, only code for the MATLAB language was developed. The viscoelastic model of the HL60 cell with 520 nodes resulted in 2080 coupled ODEs with inequality constraints.

The effect of inequality constraints on the simulations are shown in Figure 4.5. Figure 4.5(A) and (B) shows a snapshot of a simulation (taken at the same time step) after an impulse force was applied on a node (yellow), without and with constraints, respectively. The same force was applied in both simulations. Without constraints, the elongation of the Voigt element directly connected to

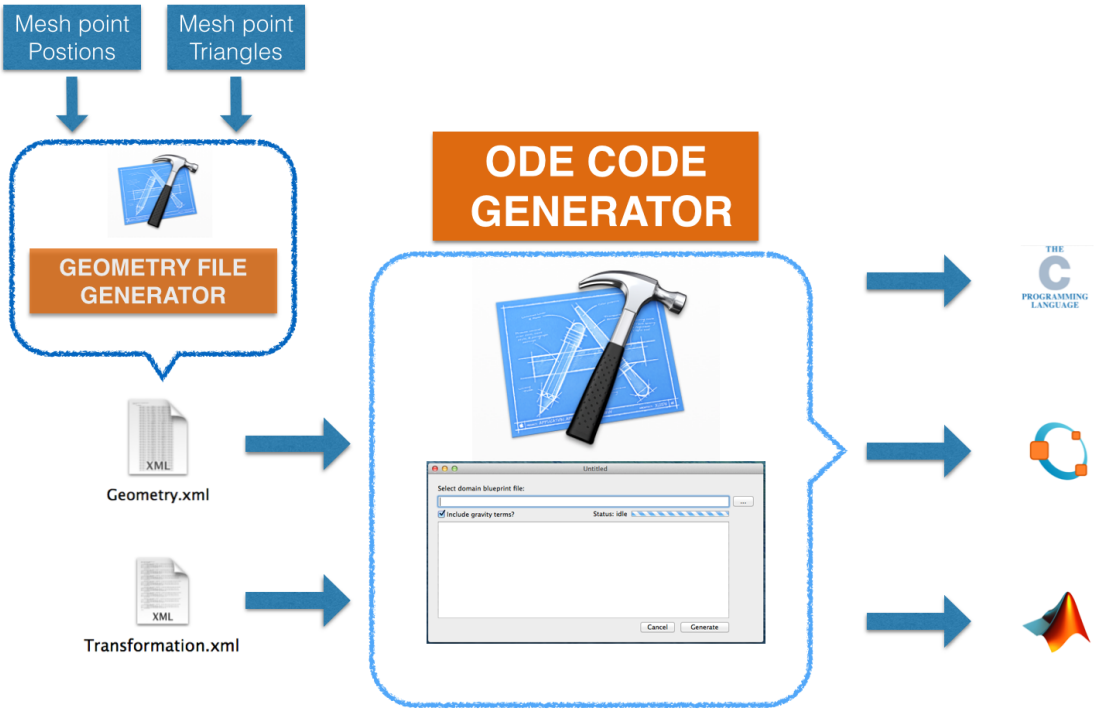

Figure 4.4: The inputs and output of the open source software developed to automatically generate the system of equations. The input for the code generator are two xml files, a geometry file and a transformation file. The geometry file was created by another open source software using output from the meshing algorithm. The resulting system of equations can be written in many languages, but for this project the equations were written in the MATLAB programming language.

the node where the impulse force is applied is very high compared to the other Voigt elements and the deformation caused by the force is locally concentrated. Moreover, when a shock wave (modeled by Friedlander equation) is applied on some nodes on the cell membrane (C), the cell turns over itself, which is an unphysical result in two dimensions. Creating the same simulations (the force kept the same in each simulation) with the constraints, leads to better results. The deformation is not localized anymore (B) and the cell does not turn over it self (D). Figure 4.6 shows snapshots of simulation where a shock wave (as

modeled by a Friedlander waveform) is applied to the viscoelastic model of the HL60 cell. The cytoplasm and the nucleus have uniform but different Voigt parameters and the force is applied on nodes indicated by red arrows. The positive part of the Friedlander waveform results in compressive stress in the cell (Figure 4.6 B - D) and the negative part of the Friedlander waveform results in tensile stress in the cell (Figure 4.6 E- G).

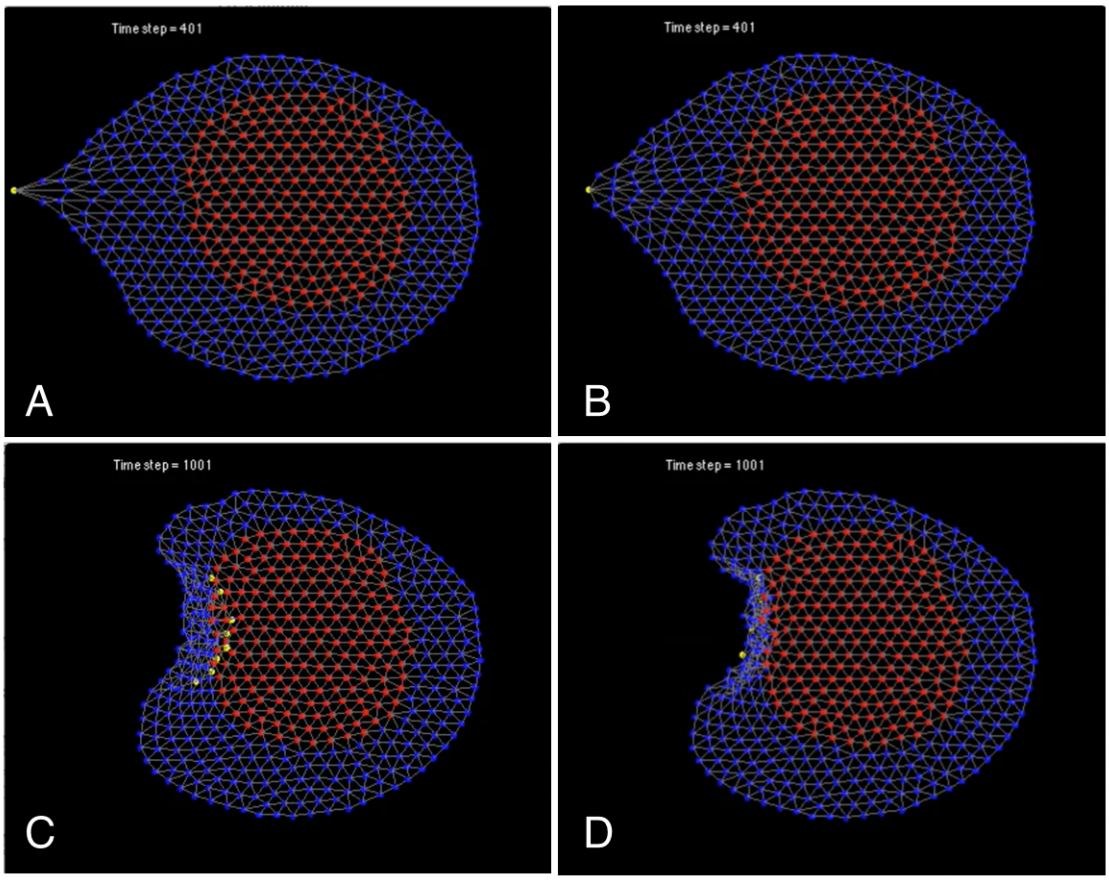

Figure 4.5: Snapshots of a simulation with (**B**, **D**) and without constraints (**A**, **C**). **(A, B)** An impulse force was applied on a node on the cell membrane. Without the constraints, the elongation of the Voigt element directly connected to the node where the impulse force is applied is very high compared to the other Voigt elements and the deformation caused by the force is locally concentrated. **(C, D)** A Friedlander force was applied on nodes (yellow) on the cell membrane. Without constraints, the cell turns over itself, which is an unphysical result in two dimensions. The cytoplasm (blue nodes) has a uniform Voigt parameter $\Theta_{cyt} = 1$ and the nucleus (red nodes) has a uniform Voigt parameter $\Theta_{nuc} = 3$.

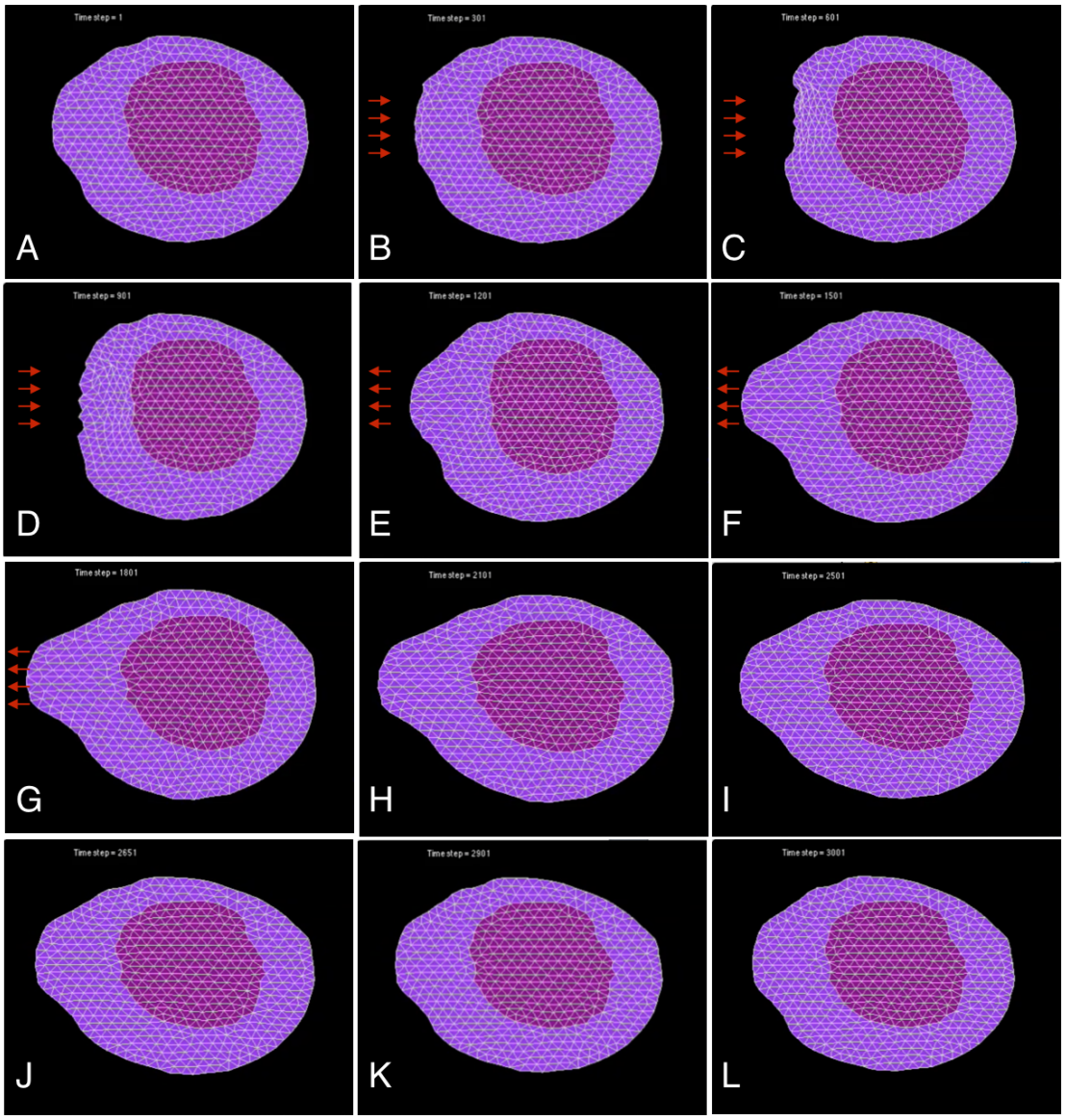

Figure 4.6: Snapshots of simulation where a shock wave is applied to a cell. The cytoplasm and the nucleus have different Voigt parameters.**(A)** Initially, there are no forces acting on the cell. **(B, C, D)** The cell is under compressive stress due to the stress wave portion of the Friedlander Force. **(E, F, G)** The cell is under tensile stress due to the tensile wave portion of the Friedlander Force. **(H, I, J, K, L)** The cell returns back to its normal shape. $\Theta_{cyt} = 1$, $\Theta_{nuc} = 3$

4.3 A Viscoelastic Model of an HL60 cell embedded in an Extracellular Matrix: Simulation and Force Estimation

In the previous simulation of the HL60 cell, all the nodes were free to move. In reality the movement of the cell is restricted by its attachment to the extracellular matrix. Figure 4.7 shows snapshots of a simulation of an HL60 cell embedded in extracellular matrix (ECM). The ECM, the cytoplasm and the nucleus all have uniform but different Voigt parameters. This model of the HL60 cell embedded in its local environment has $1,871$ nodes and $10,912$ Voigt elements. The top, bottom and the right edge of the ECM are fixed and a Friedlander force is applied on the left edge of the ECM (indicated by red arrows). Figure 4.8 shows the Friedlander force profile applied on each node on the left edge of the ECM. The positive force results in compressive stress on the model and the negative force results in tensile stress on the model. The force on each node in each coordinate direction can be calculated using Equation 3.1 and the force at any coordinate in the viscoelastic model can be estimated using bilinear interpolation. Figure 4.9 and 4.10 show snapshots of dimensionless force in the viscoelastic model during the simulation in ordinate (y-direction) and abscissa (x-direction), respectively. Figure 4.11 and 4.12 show the same snapshots with a close up of the HL60 cell and with a different force resolution in the case of Figure 4.11. This model can also be used to simulate the formation and subsequent rupture of bubbles in the the local environment of the cell.

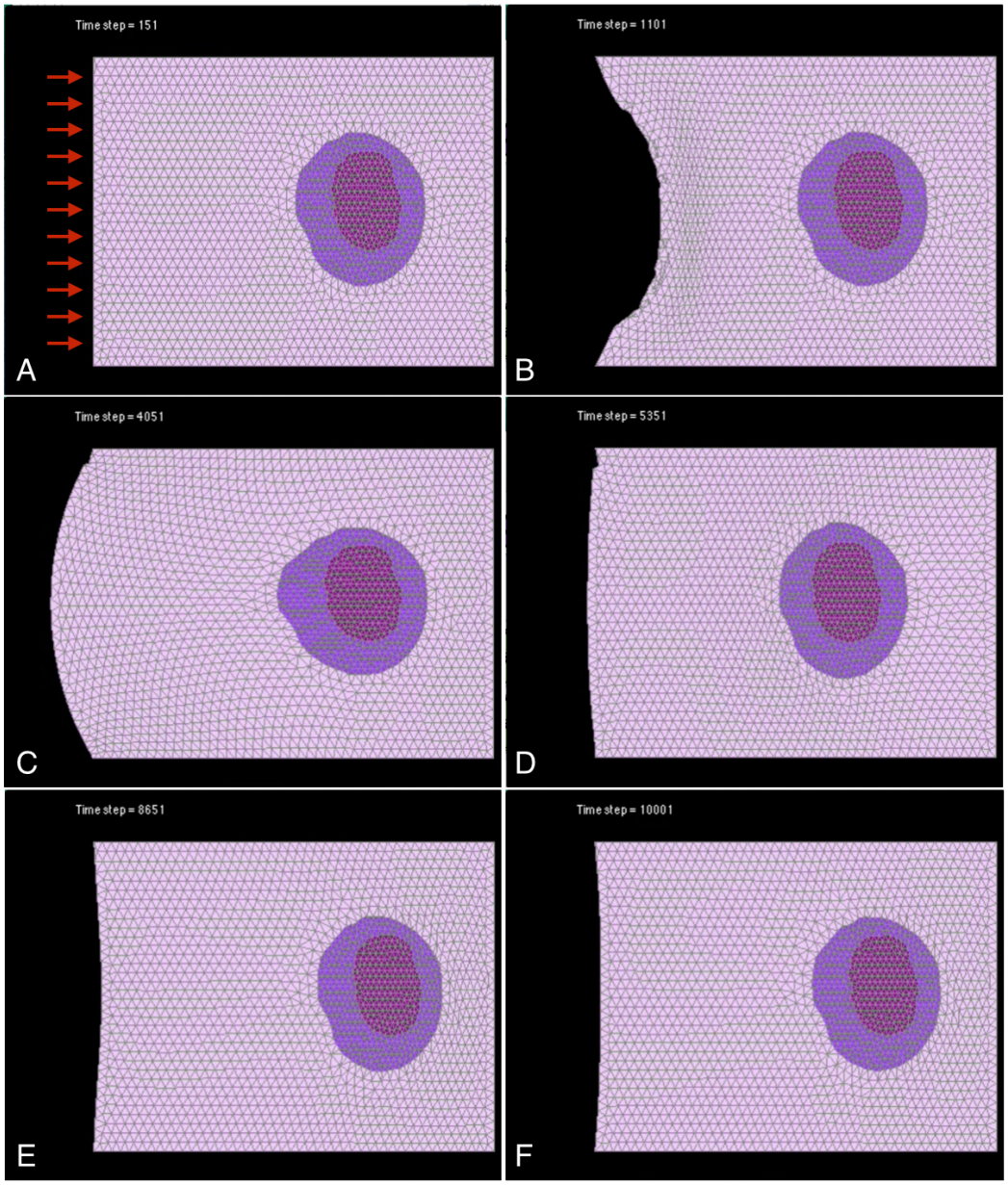

Figure 4.7: Snapshots of a simulation of an HL60 cell embedded in extracellular matrix (ECM). The ECM, the cytoplasm and the nucleus all have uniform but different Voigt parameters. $\Theta_{ECM} = 1$, $\Theta_{cytoplasm} = 2$ and $\Theta_{nucleus} = 5$. The model has $1,871$ nodes and $10,912$ Voigt elements. The top, bottom and the right edge of the ECM are fixed and a Friedlander force is applied on the left edge of the ECM (indicated by red arrows). **(A)** Before the force is applied. **(B)** Immediately after the Friedlander force is applied. The model is under compressive stress. **(C)** The model is under tensile stress. **(D - F)** The model returns to its original shape.

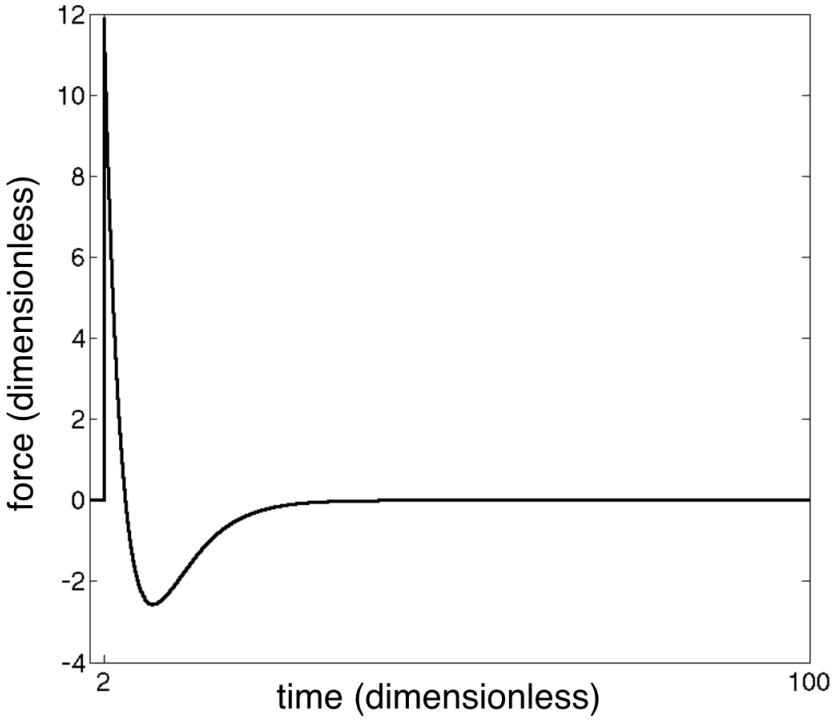

Figure 4.8: Friedlander force profile that is applied on each node on the left edge of ECM in the simulation corresponding to Figure 4.7. The positive force results in compressive stress and the negative force results in tensile stress.

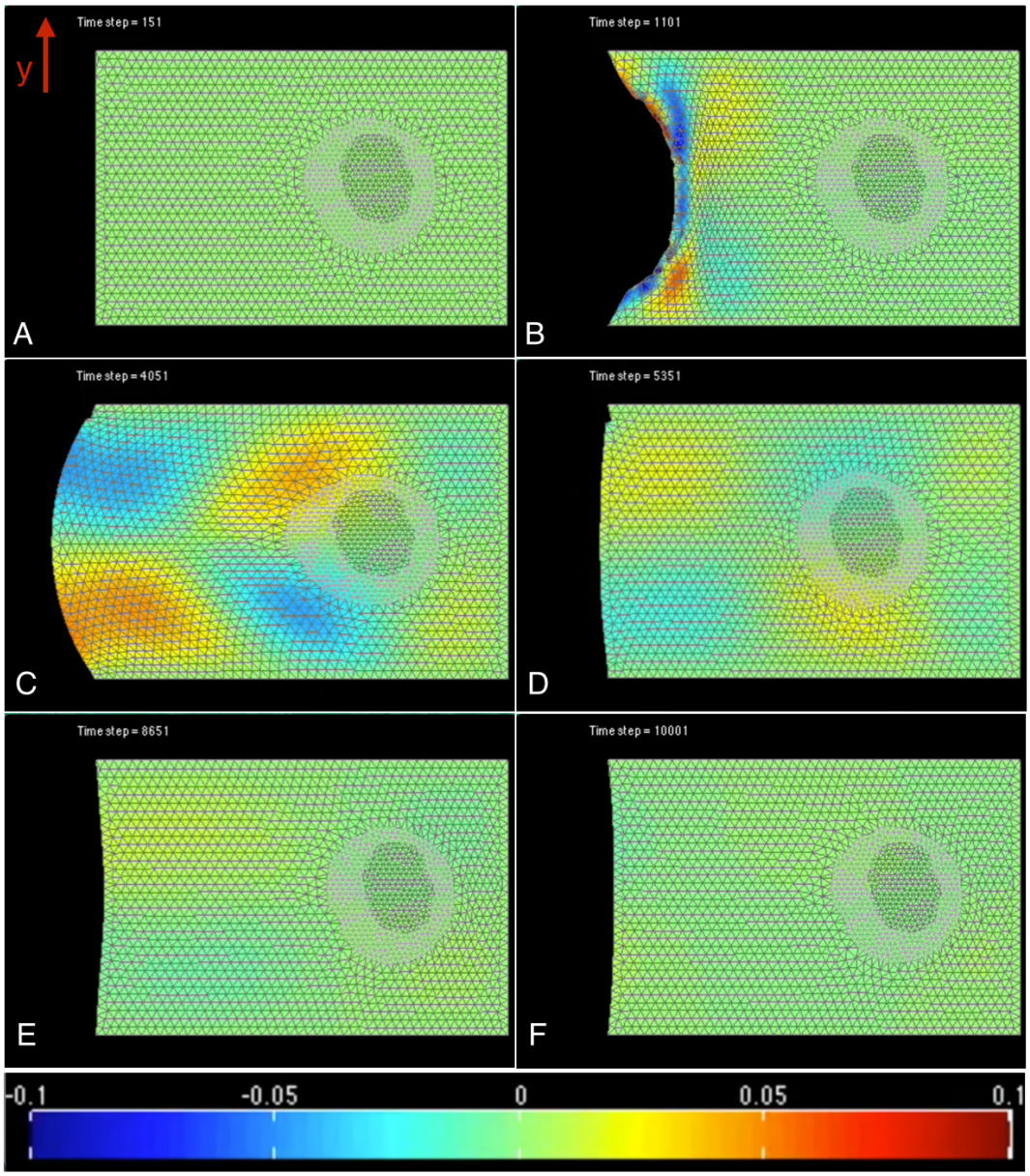

Figure 4.9: Snapshots of dimensionless force in ordinate (or y-direction) in a simulation of an HL60 cell embedded in extracellular matrix (ECM). The color bar represents the dimensionless force. The ECM, the cytoplasm and the nucleus all have uniform but different Voigt parameters. $\Theta_{ECM} = 1$, $\Theta_{cytoplasm} = 2$ and $\Theta_{nucleus} = 5$. The model has $1,871$ nodes and $10,912$ Voigt elements. The top, bottom and the right edge of the ECM are fixed and a Friedlander force is applied on the left edge of the ECM. **(A)** Before the force is applied. **(B)** Immediately after the Friedlander force is applied. The model is under compressive stress. **(C)** The model is under tensile stress. **(D - F)** The model returns to its original shape.

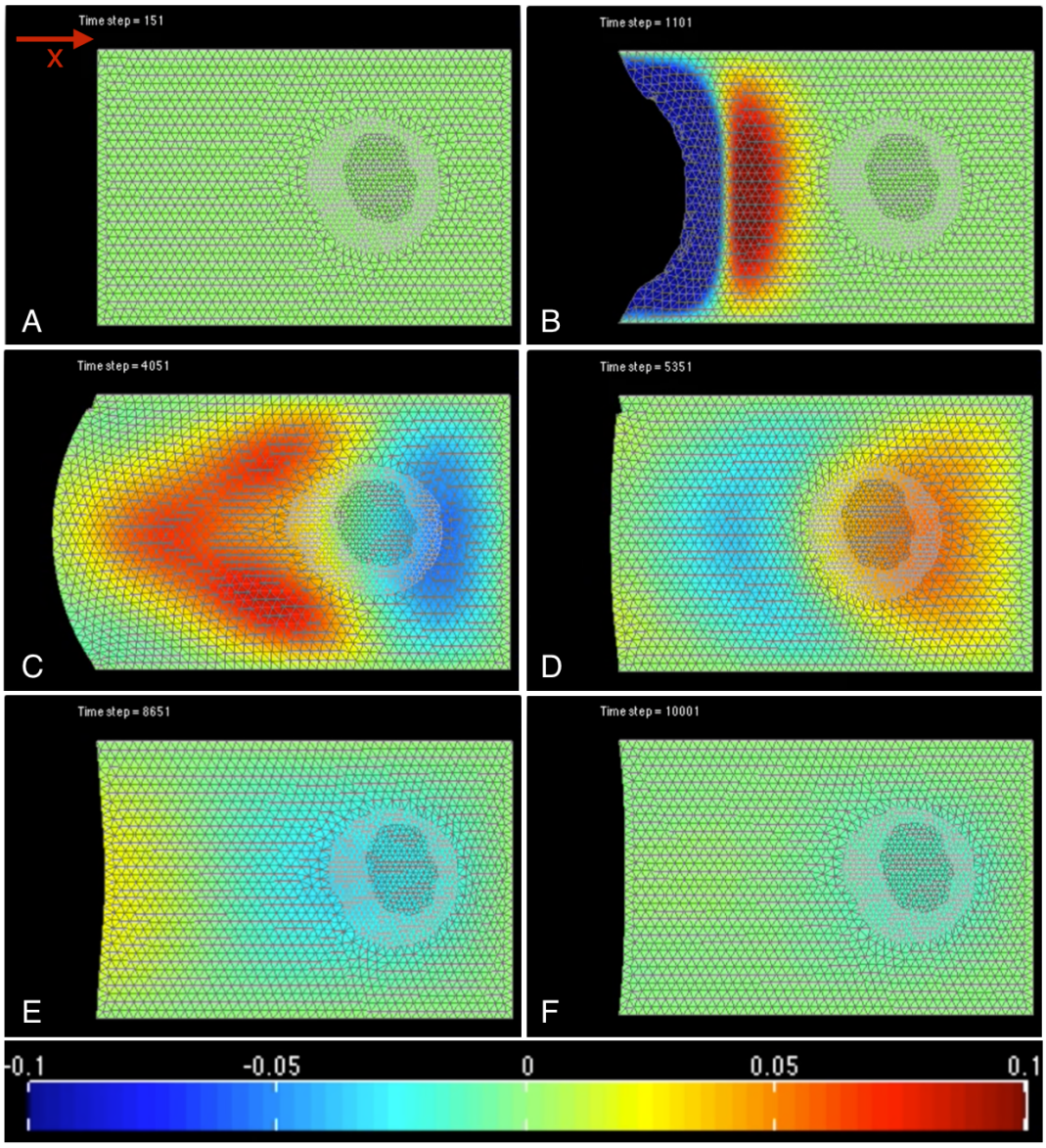

Figure 4.10: Snapshots of dimensionless force in abscissa (or x-direction) in a simulation of an HL60 cell embedded in extracellular matrix (ECM). The color bar represents the dimensionless force. The ECM, the cytoplasm and the nucleus all have uniform but different Voigt parameters. $\Theta_{ECM} = 1$, $\Theta_{cytoplasm} = 2$ and $\Theta_{nucleus} = 5$. The model has $1,871$ nodes and $10,912$ Voigt elements. The top, bottom and the right edge of the ECM are fixed and a Friedlander force is applied on the left edge of the ECM. **(A)** Before the force is applied. **(B)** Immediately after the Friedlander force is applied. The model is under compressive stress. **(C)** The model is under tensile stress. **(D - F)** The model returns to its original shape.

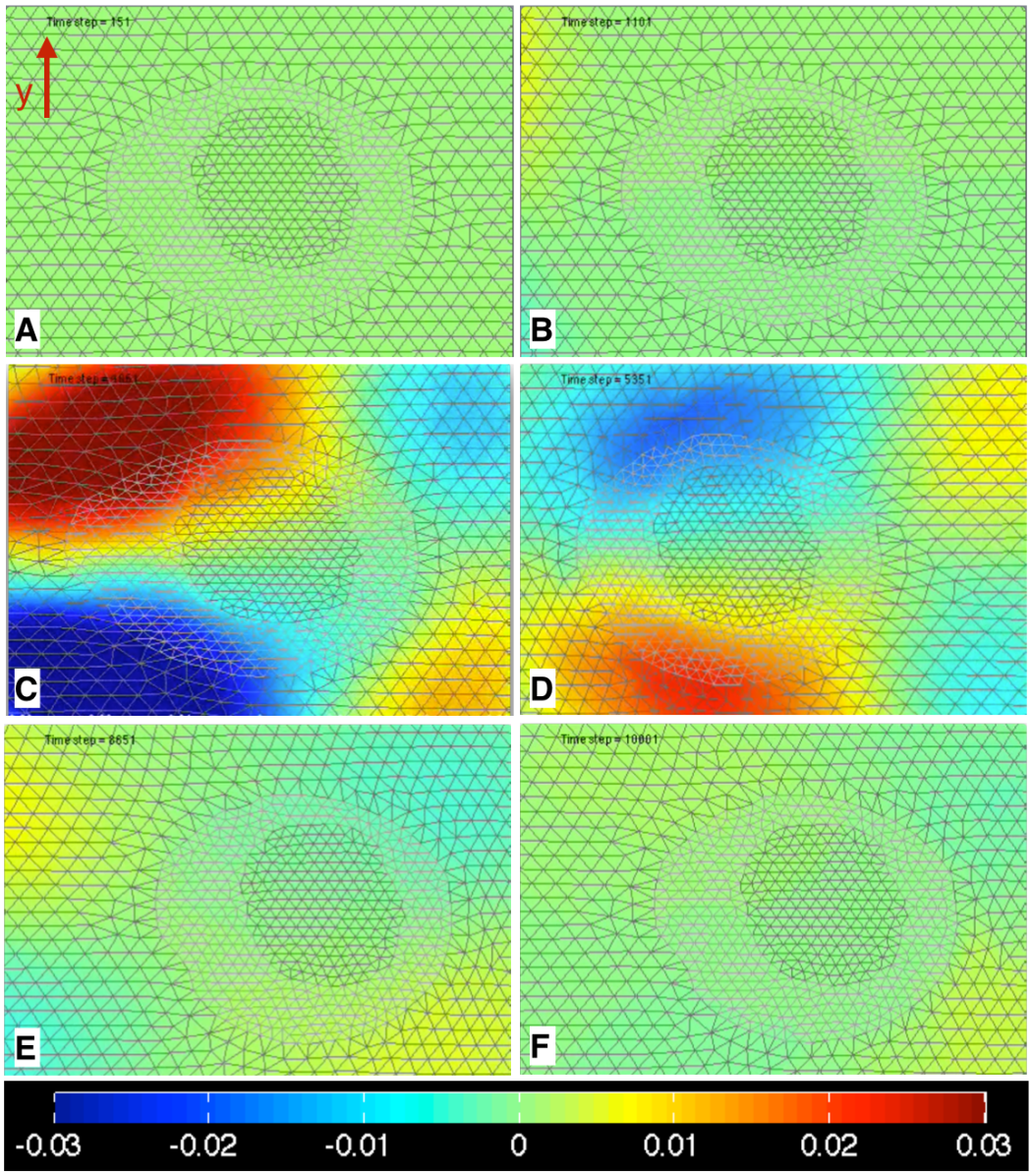

Figure 4.11: Snapshots of dimensionless force in ordinate (or y-direction) in a simulation of an HL60 cell embedded in extracellular matrix (ECM). Each snapshot **(A - F)** corresponds to the same time step as in Figure 4.9 but shows a close up of HL60 cell and a different force resolution. The color bar represents the dimensionless force. The ECM, the cytoplasm and the nucleus all have uniform but different Voigt parameters. $\Theta_{ECM} = 1$, $\Theta_{cytoplasm} = 2$ and $\Theta_{nucleus} = 5$.

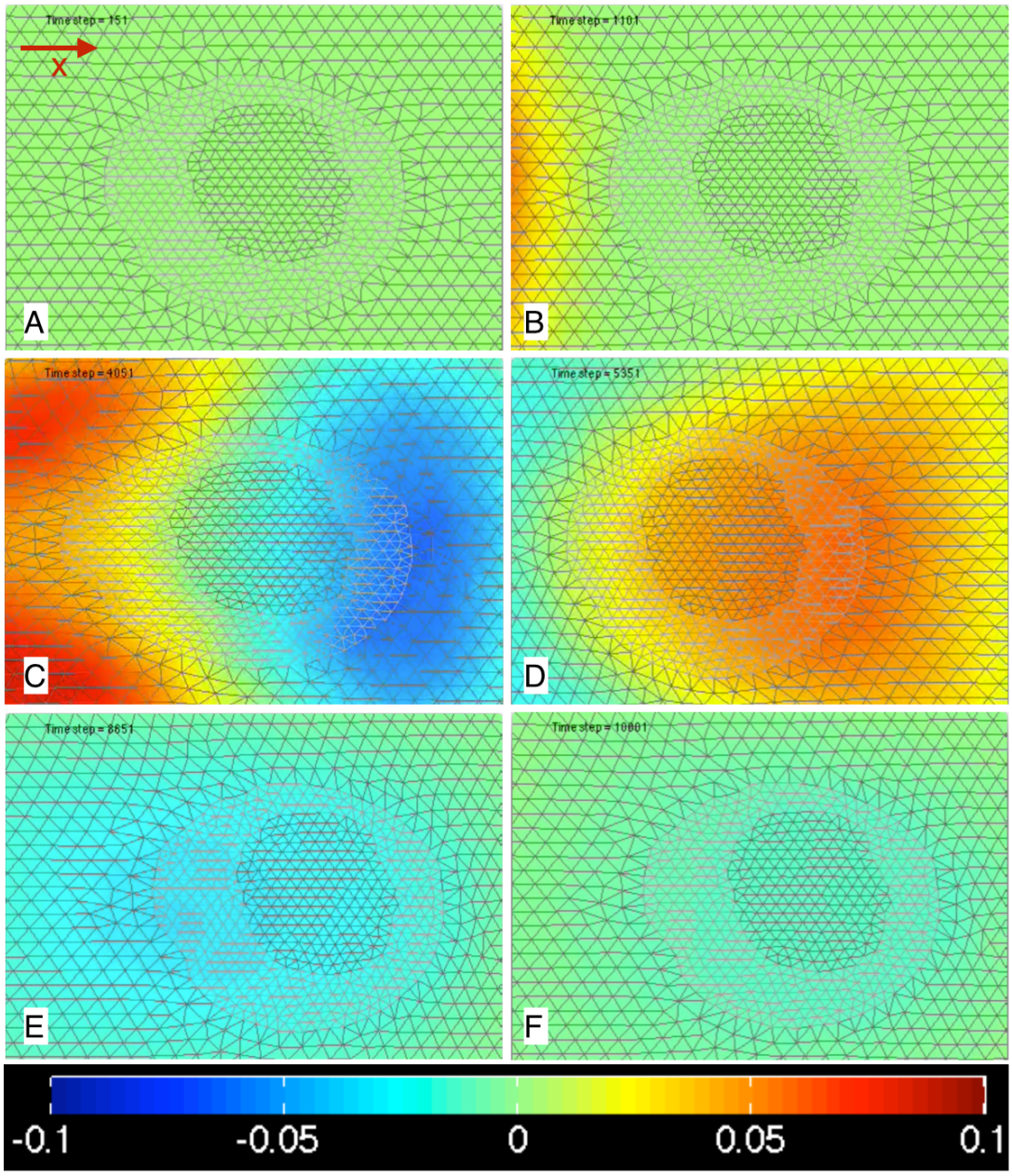

Figure 4.12: Snapshots of dimensionless force in abscissa (or x-direction) in a simulation of an HL60 cell embedded in extracellular matrix (ECM). Each snapshot **(A - F)** corresponds to the same time step as in Figure 4.10 but shows a close up of HL60 cell. The color bar represents the dimensionless force. The ECM, the cytoplasm and the nucleus all have uniform but different Voigt parameters. $\Theta_{ECM} = 1$, $\Theta_{cytoplasm} = 2$ and $\Theta_{nucleus} = 5$.

4.4 The Effect of Damping Ratio on the Viscoelastic Model.

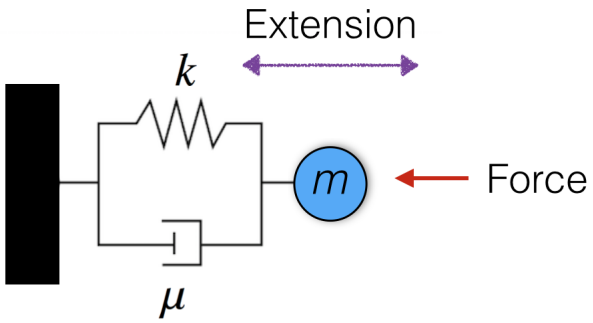

Figure 4.13: Schematic of a traditional mass-spring-damper system which is equivalent to a Voigt element with one edge fixed and the other edge connected to a mass m.

A single Voigt element with one edge fixed and the other edge free to move with mass m kg is the equivalent to a traditional mass-spring-damper system. The damping ratio is a dimensionless factor that governs the how the oscillations (extension of spring) in the system decay after a force is applied on the free end of the Voigt element. The damping ratio is defined by Equation 4.1. If $\zeta < 1$, the system is described as being underdamped and extension will decay with oscillations. If $\zeta > 1$, the system is described as being overdamped and extension will decay exponentially (without oscillations). Equation 4.2 shows the relationship between the Voigt parameter and the damping ratio for a unit mass.

$$\zeta = \frac{\mu}{2\sqrt{k}} \tag{4.1}$$

$$\Theta = 4\zeta^2 \tag{4.2}$$

In the viscoelastic model developed for an HL60 cell, multiple Voigt elements are connected in a complex arrangement but the damping ratio for a single Voigt element governs the reaction of the model to perturbations up to a large extent. Figure 4.14 ($\zeta = 0.32$) and 4.15 ($\zeta = 3.54$) show snapshots of dimensionless force in ordinate (or y-direction) in a simulation of an HL60 cell after a Friedlander force is applied. In both simulations, the model is subjected to the same force profile. In the former, larger forces are observed than in the latter. Moreover, in the former the forces decay with oscillations. Many simulations were conducted with different ratios of the spring parameter and the damping parameter. Figure 4.16 and 4.17 show plots of dimensionless force on each node in the model (ordinate or y-direction) against dimensionless time for these simulations. In cases where $\zeta < 1$, the forces in ordinate (or y-direction) decay with oscillations, as in the case of an underdamped mass-spring-damper system. Similarly, it could be expected that for cases when $\zeta > 1$, the forces would decay without oscillations, as in the case of an over-damped mass-spring-damper system. However, oscillations as forces decay are still observed, but the amplitude of the oscillations is much lower than in the cases when $\zeta < 1$. The oscillations are believed to be present due to the complex spatial arrangement of Voigt elements connected together. The same phenomena is observed in abscissa (or x-direction) as well and plots of dimensionless force on each node in the model (abscissa or x-direction) against dimensionless time for the same simulations can be found in the Appendix (Figure A.5 and A.4).

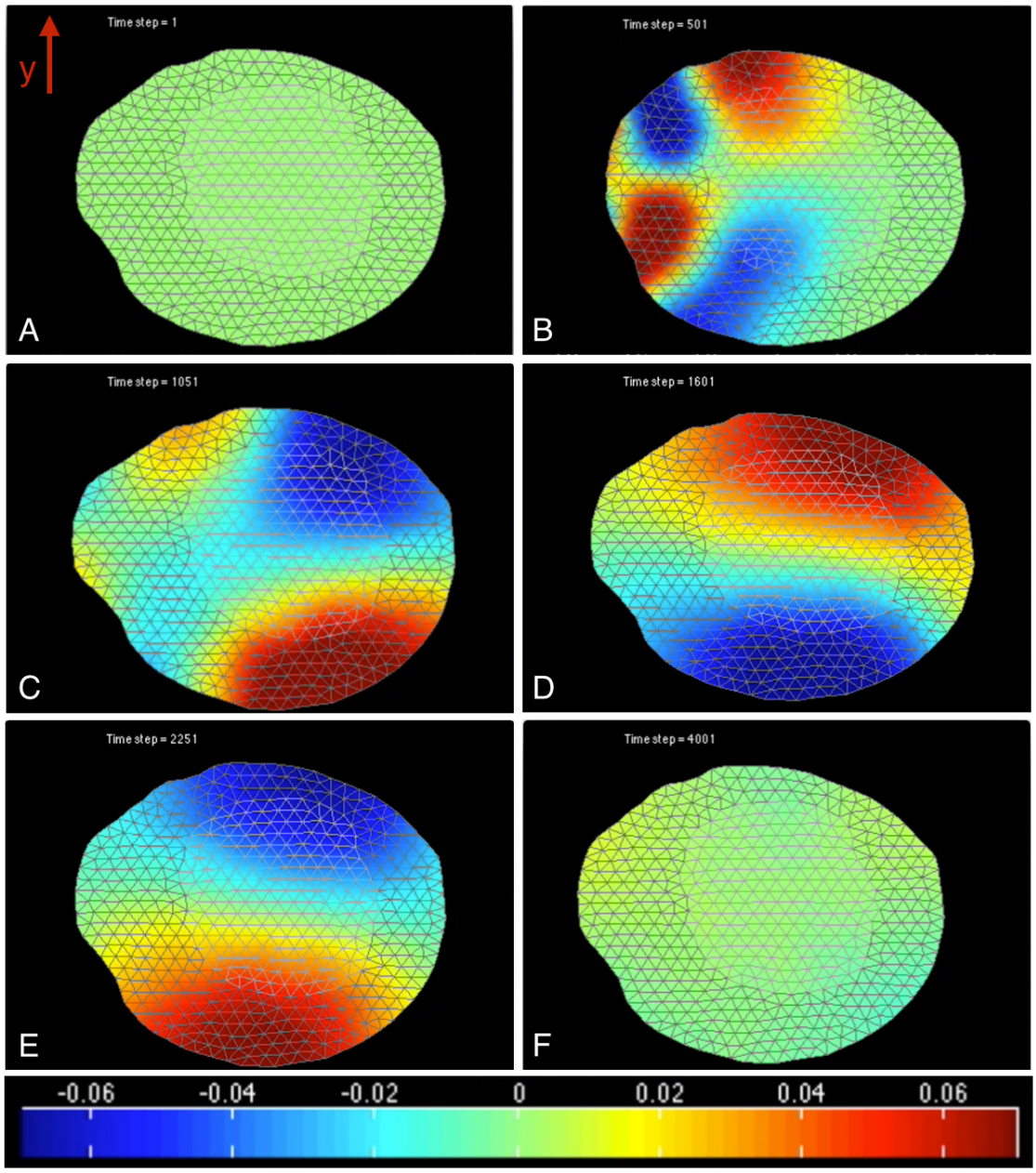

Figure 4.14: Snapshots of dimensionless force in ordinate in a simulation of an HL60 cell after a Friedlander force is applied. The cytoplasm and the nucleus have uniform and identical Voigt parameters. $\mu = 2$, $k = 10$, $\tau = 0.2$, $\zeta = 0.32$. **(A)** Before the force is applied. **(B)** Immediately after the Friedlander force is applied. The cell is under compressive stress. **(C - D)** The cell is under tensile stress. **(E - F)** The cell returns to its original shape.

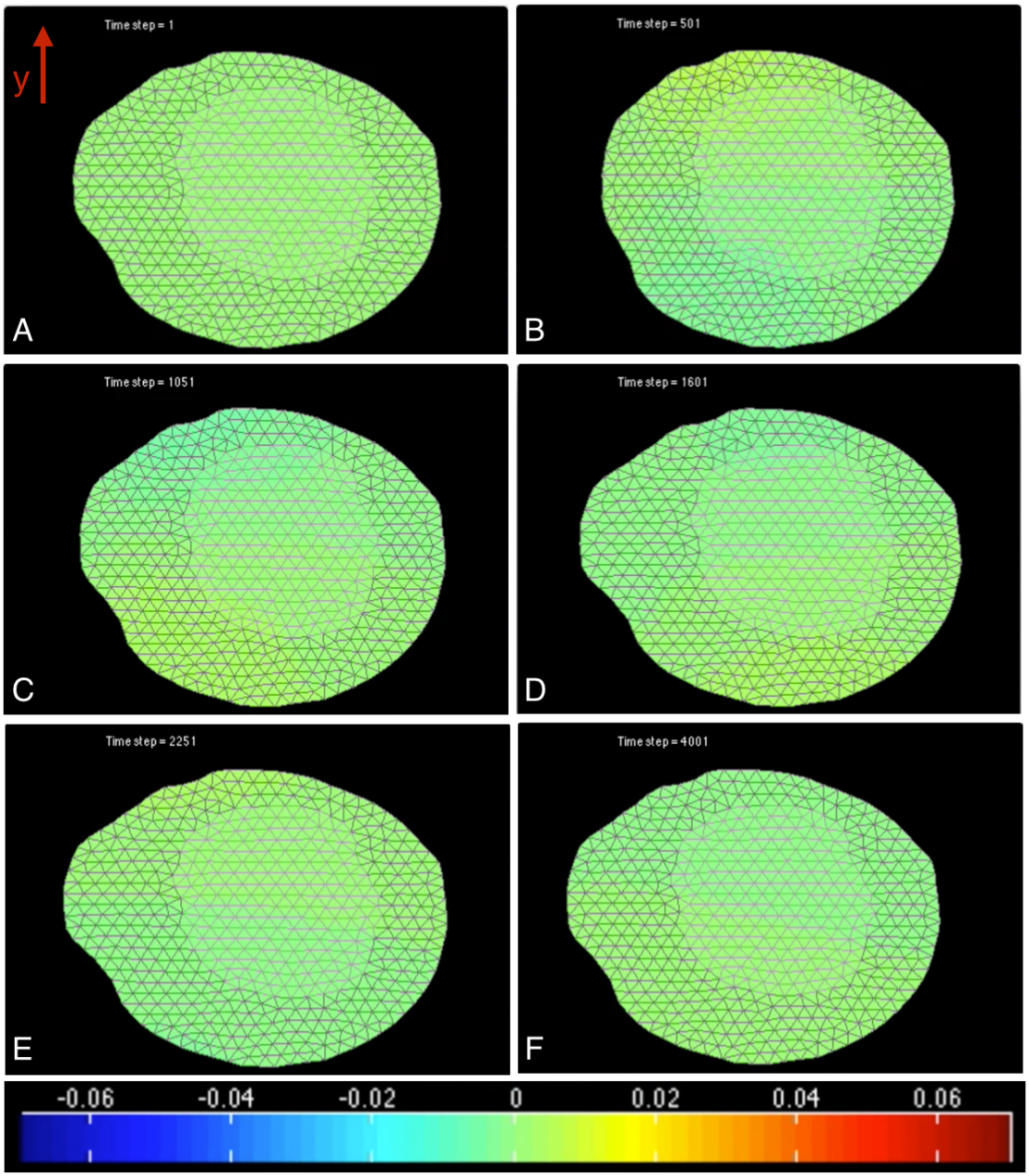

Figure 4.15: Snapshots of dimensionless force in ordinate in a simulation of an HL60 cell after a Friedlander force is applied. The cytoplasm and the nucleus have uniform and identical Voigt parameters. $\mu = 10$, $k = 2$, $\tau = 5$, $\zeta = 3.54$. **(A)** Before the force is applied. **(B)** Immediately after the Friedlander force is applied. The cell is under compressive stress. **(C - D)** The cell is under tensile stress. **(E - F)** The cell returns to its original shape.

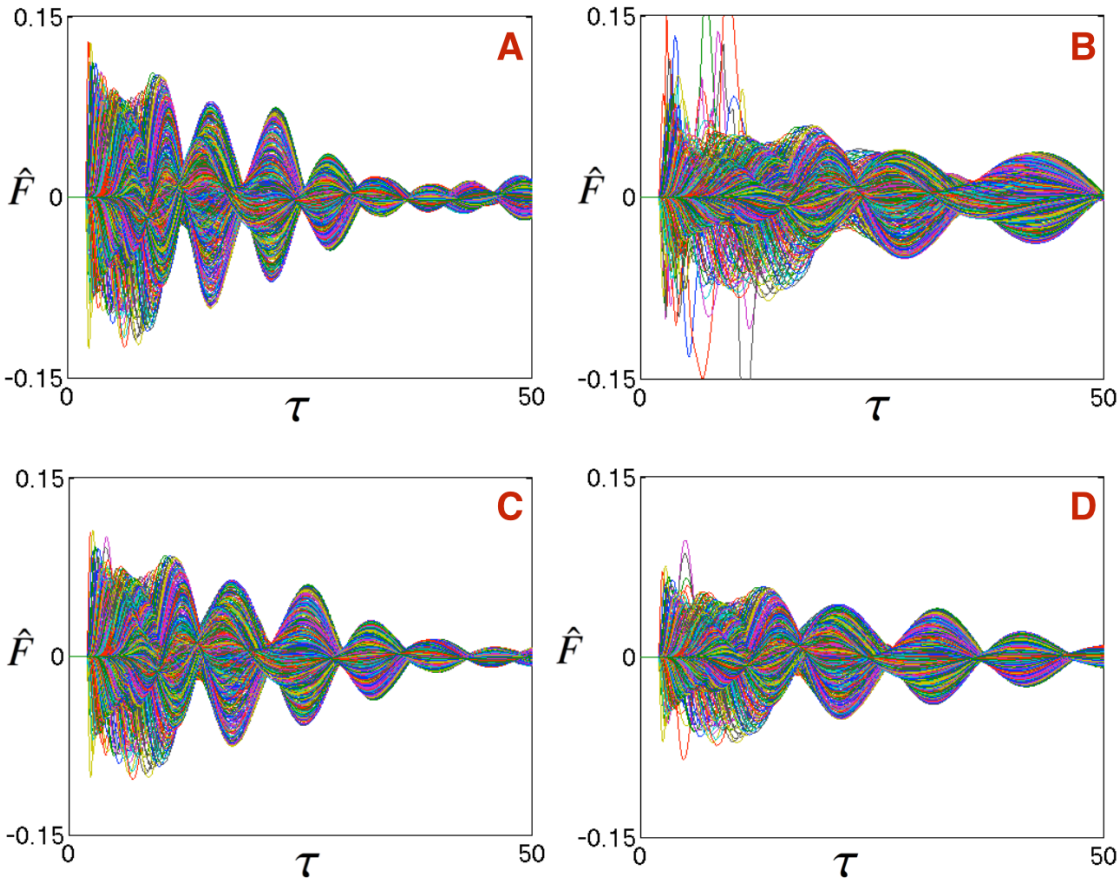

Figure 4.16: Dimensionless force (ordinate or y-direction) against dimensionless time for simulations of HL60 cells with different Voigt parameters. A Friedlander force is applied at $\tau = 2$. The cytoplasm and the nucleus had uniform and identical parameters in each case. **(A)** $\mu = 2$, $k = 10$, $\Theta = 0.4$, $\zeta = 0.32$. **(B)** $\mu = 1$, $k = 2$, $\Theta = 0.5$, $\zeta = 0.35$. **(C)** $\mu = 2$, $k = 7$, $\Theta = 0.57$, $\zeta = 0.38$. **(D)** $\mu = 2$, $k = 4$, $\Theta = 1$, $\zeta = 0.5$. All parameters are dimensionless.

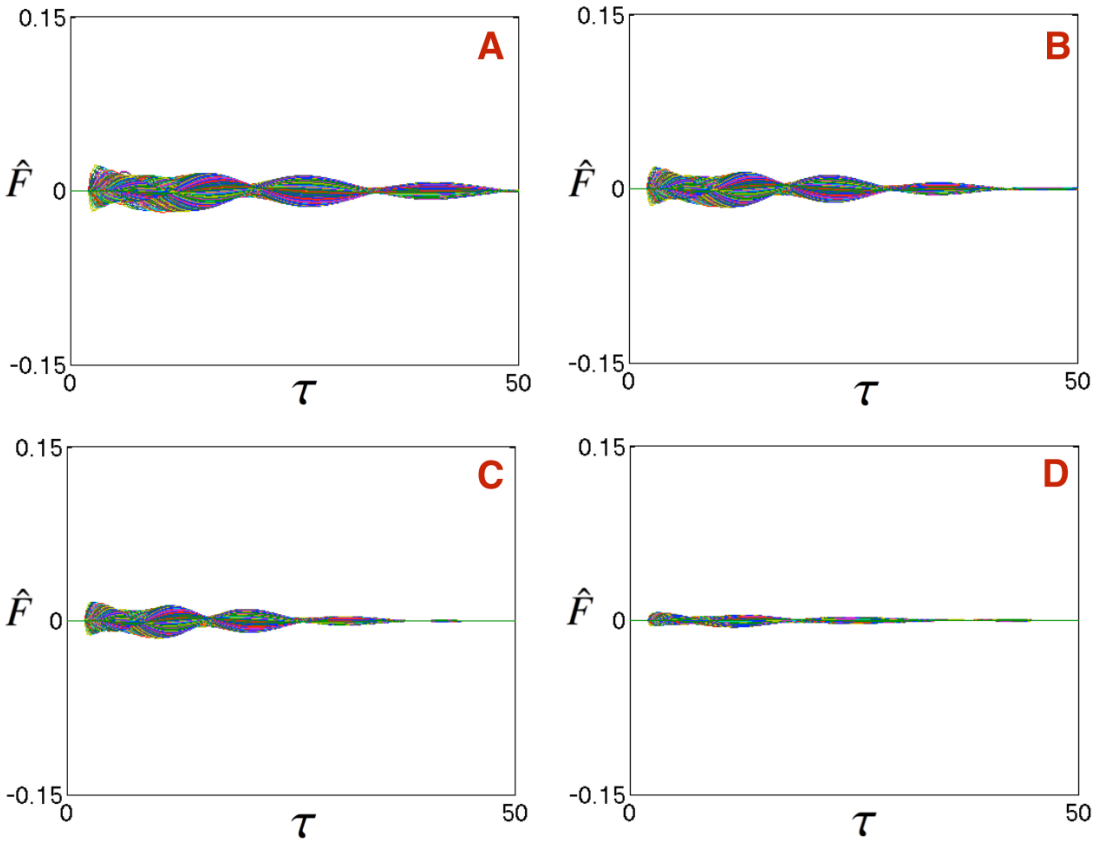

Figure 4.17: Dimensionless force (ordinate or y-direction) against dimensionless time for simulations of HL60 cells with different Voigt parameters. A Friedlander force is applied at $\tau = 2$. The cytoplasm and the nucleus had uniform and identical parameters in each case. **(A)** $\mu = 4$, $k = 2$, $\Theta = 8$, $\zeta = 1.41$. **(B)** $\mu = 6$, $k = 3$, $\Theta = 12$, $\zeta = 1.73$. **(C)** $\mu = 8$, $k = 4$, $\Theta = 16$, $\zeta = 2$. **(D)** $\mu = 10$, $k = 2$, $\Theta = 50$, $\zeta = 3.54$. All parameters are dimensionless.

4.5 A Viscoelastic Model of an Irregular Shaped Cell

A viscoelastic model of a cell with irregular shape (an astrocyte) was created. Figure 4.18 shows the image of the astrocyte and the signed distance function of the cell. The nucleus was not meshed in this simulation and the model had a uniform Voigt parameter ($\Theta = 1$). This model had 427 nodes and 1708 coupled ODE's with inequality constraints. Figure 4.19 shows snapshots of a simulation of applying a force to the body of a viscoelastic model of an astrocyte and Figure 4.20 show snapshots of simulation of applying a force to a dendrite. The meshing algorithm was able to mesh the geometry of the irregular shape, but some cell area was lost in the meshing procedure (some of the dendrites were not completely captured by the viscoelastic model). The fraction of total area of the cell image that is captured in the viscoelastic model could be increased if a high resolution image is used in future studies. Some loss of cell area still might be expected if the dendrites are very thin but this is not expected to substantially limit the ability to estimate forces in other parts of the simulation, where the cell area is captured fully by the model.

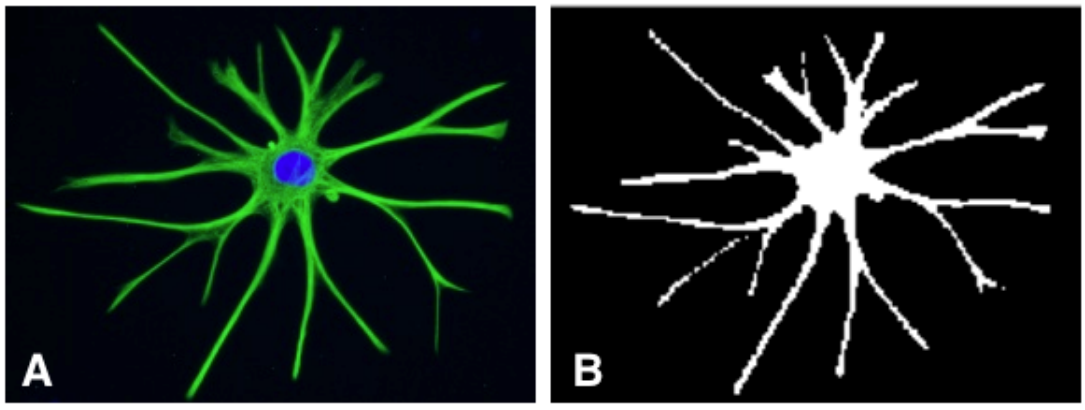

Figure 4.18: **(A)** Image of an astrocyte. **(B)** Signed Distance Function of an astrocyte.

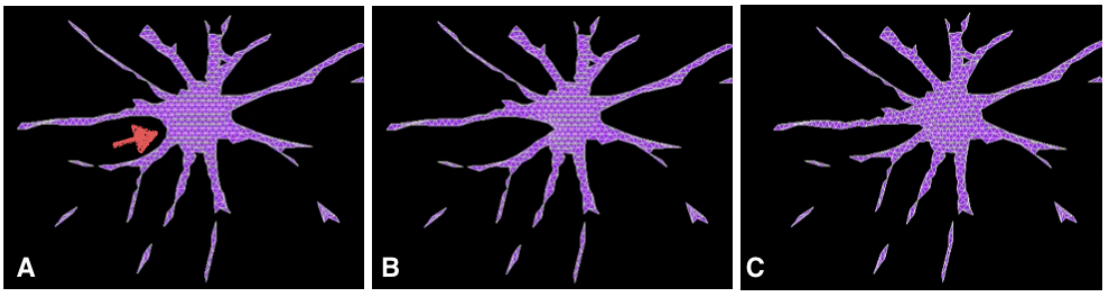

Figure 4.19: Snapshots of simulation of applying a force to the body of a viscoelastic model of an astrocyte. **(A)** Before the force is applied. The arrow indicates the site of the force. **(B)** Some time steps after the force is applied. **(C)** Many time steps after the force is applied.

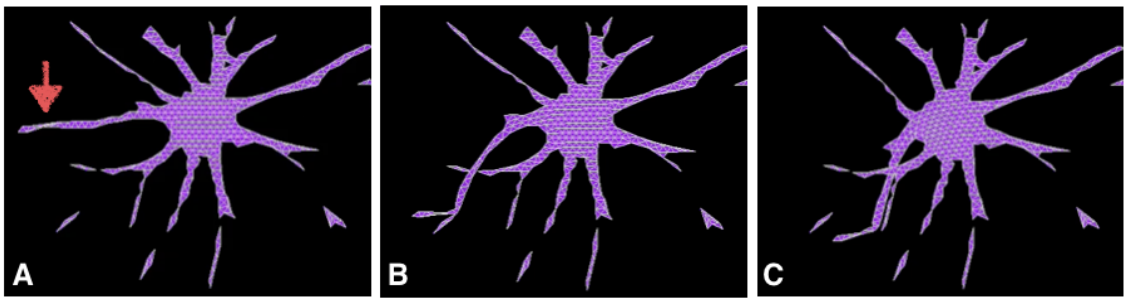

Figure 4.20: Snapshots of simulation of applying a force to a dendrite of a viscoelastic model of an astrocyte. **(A)** Before the force is applied. The arrow indicates the site of the force. **(B)** Some time steps after the force is applied. **(C)** Many time steps after the force is applied.

4.6 Developing an Accurate Model Using Optimization Techniques

Synthetic data was created after a shock wave was applied to a viscoelastic model of an HL60 cell with different Voigt parameters in the nucleus and the cytoplasm. A time step of 0.01 was used in creating this synthetic data and synthetic parameters were $\Theta_{cyt} = 1$ and $\Theta_{nuc} = 3$. The optimization was initialized with the parameters $\Theta_{cyt} = 10$ and $\Theta_{nuc} = 10$. An optimization time step of 0.1 was used and only 10% of the nodes were considered in the optimization procedure, which were equally distributed in the cytoplasm and the nucleus. The optimization was done in MATLAB using the fminsearch function. The optimization ended after 706 function evaluations and the second norm of the difference between the resultant parameters (optimization parameters) and the synthetic parameters was less than $1 \cdot 10^{-4}$. There is no significant difference between two simulations, when the second norm of the difference between parameters of the two simulations is $1 \cdot 10^{-1}$. Thus, the factor of $1 \cdot 10^{-4}$ was deemed more than sufficient to qualify a successful optimization. Figure 4.21 shows snapshots (at the same time step) of simulations of the viscoelastic model that were created using intermediate parameters (taken at different iterations of the optimization procedure) from the optimization run. Figure 4.21 (A) shows a snapshot of simulation as run with the initial parameters, (F) shows a snapshot of a simulation as run with parameters that were obtained at the end of the optimization run.

To look at the effect of different optimization time steps (size of set t^{opt}) and different number of nodes in the objective function (size of set p^{opt}), optimization runs were done with different number of nodes in objective function and

different optimization time steps. For each case (certain optimization time step and percentage of node in objective function), 40 trials were run. Of these runs, an optimization was considered successful if $\|\Theta_{syn} - \Theta_{opt}\| \leqslant 1 \cdot 10^{-4}$ for all parameters. Also, the starting parameters for the nucleus and cytoskeleton were chosen randomly. The time step for the synthetic data time step was 0.01 and the cytoskeleton and the nucleus had uniform but different Voigt parameters. Figure 4.22 and Figure 4.23 shows the plot of the percentage of successful optimization runs against percentage of nodes considered in objective function and optimization time step, respectively. Using different number of nodes in the objective function or using a large optimization time step did not seem to have an effect on the outcome of a successful optimization. Moreover, Voigt parameters of the nucleus and the cytoskeleton were estimated successfully in alteast 50% of the optimization runs for each case considered.

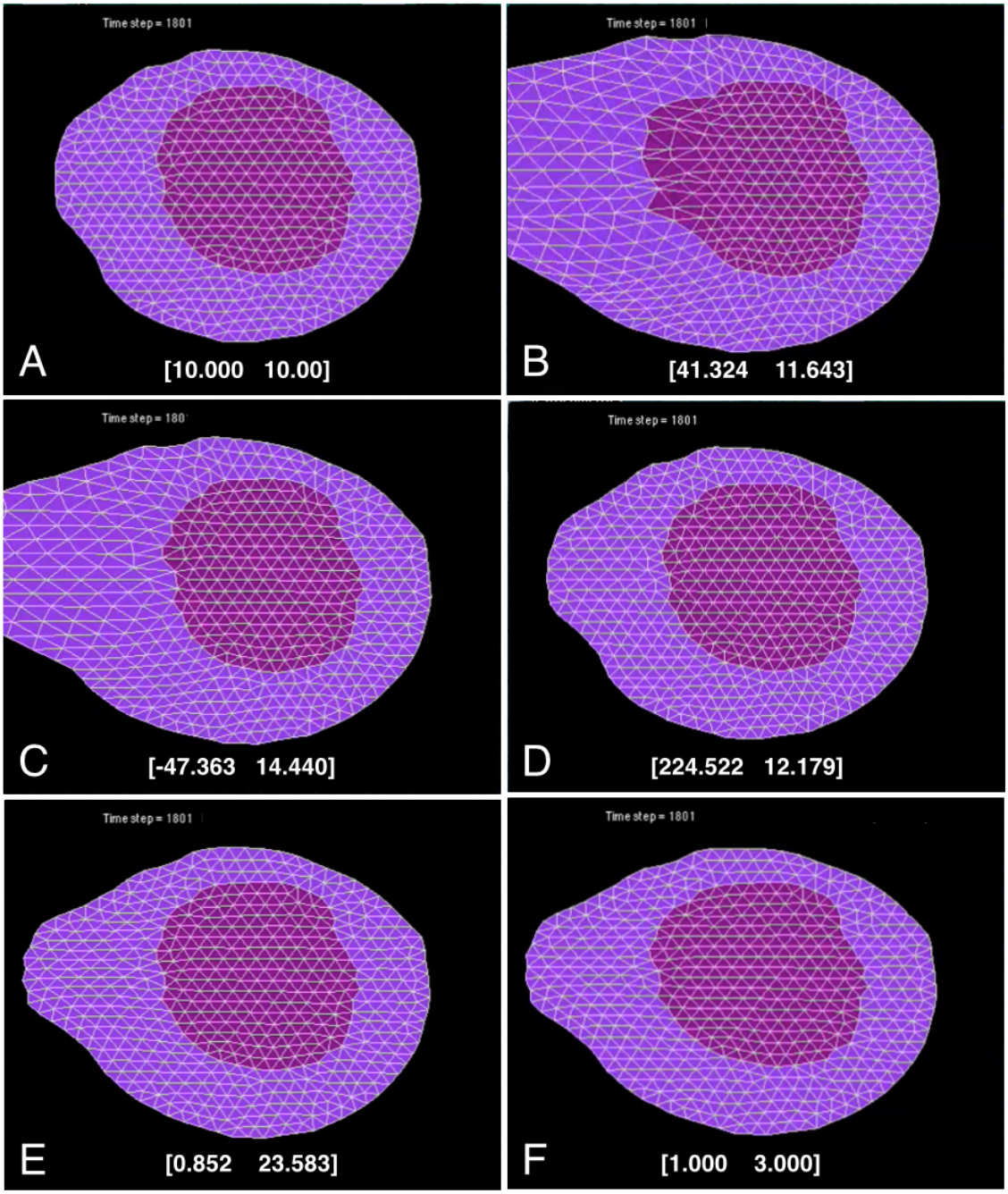

Figure 4.21: Snapshots of simulations conducted with different Voigt element parameters. All the snapshots show the same time step during the simulation. **(A)** The starting parameters supplied to the optimization algorithm $\Theta_{cyt} = 10$, $\Theta_{nuc} = 10$. **(B, C, D, E)** Simulation performed at parameters taken at different iterations of the optimization procedure. **(F)** The parameters obtained from the optimization algorithm when the optimization ended. These match the synthetic parameters, $\Theta_{cyt} = 1$, $\Theta_{nuc} = 3$.

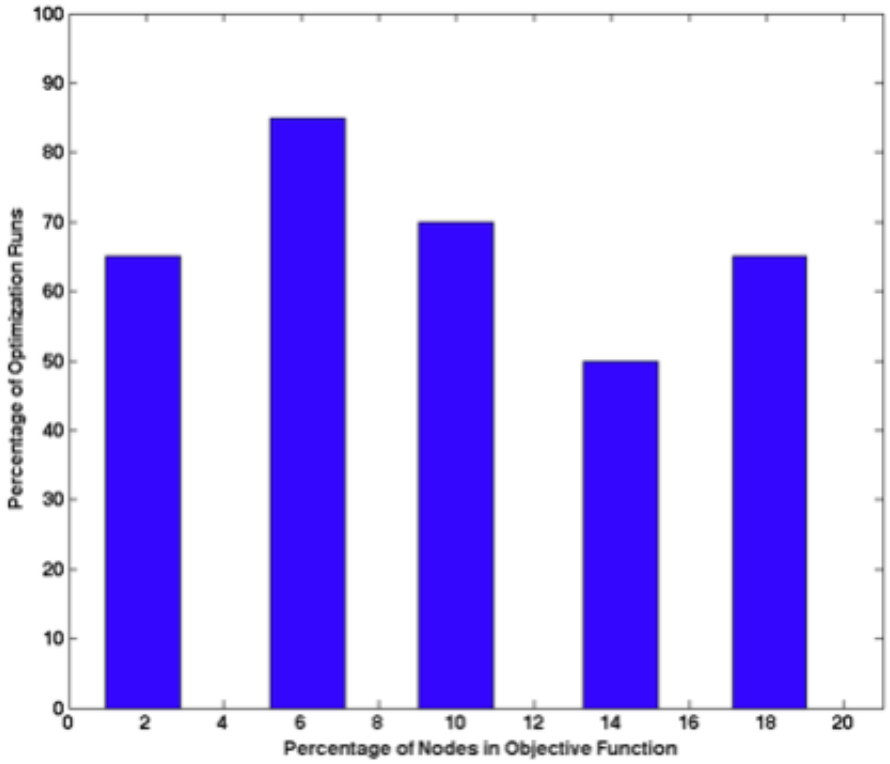

Figure 4.22: Plot of percentage of successful optimization runs agains percentage of nodes in the objective function. 40 optimization runs were conducted for each case. An optimization run was considered a success if $\|\Theta_{syn} - \Theta_{opt}\| \leqslant 1 \cdot 10^{-4}$ for all parameters.

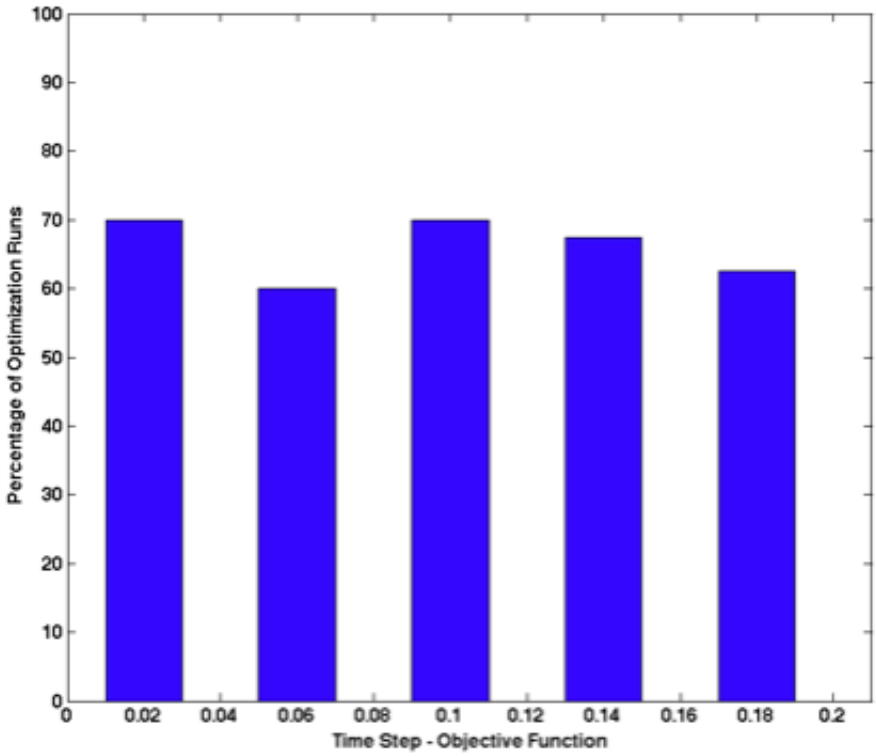

Figure 4.23: Plot of percentage of successful optimization runs agains time step in the objective function. 40 optimization runs were conducted for each case. An optimization run was considered a success if $||\Theta_{syn} - \Theta_{opt}|| \leqslant 1 \cdot 10^{-4}$ for all parameters.

4.7 Choosing an Edge Size Function: Balancing Computational Expense and Model Resolution

Figure 4.24 show three viscoelastic models of the HL60 cell (without nucleus) meshed using different element size functions, which implicitly governs the number of nodes in the model. The models have (1) 540 nodes, (2) 194 nodes and (3) 61 nodes. Simulations were created where the same impulse force was applied on three different models and snapshots of the resulting deformation is shown. The model with 540 nodes is able to capture the deformation of the cell membrane as a result of the impulse force but the model with only 61 nodes, is not able to capture a similar change in shape of the cell membrane. A model with a greater number of nodes will be able to capture small changes in shape but is more computationally expensive, as there are a greater number of ODEs to solve and moreover because the inequality constraints are $O(n^2)$, where n is the number of nodes. A model with a smaller number of nodes, on the other hand, is less computationally expensive but might not be able to capture small changes in cell shape. For simulations created in this study the edge function, which implicitly governs the number of nodes in the viscoelastic model, was chosen arbitrarily. When experimental data is available, the edge size function can be chosen to balance computational expense with the ability to model minute changes in cell shape.

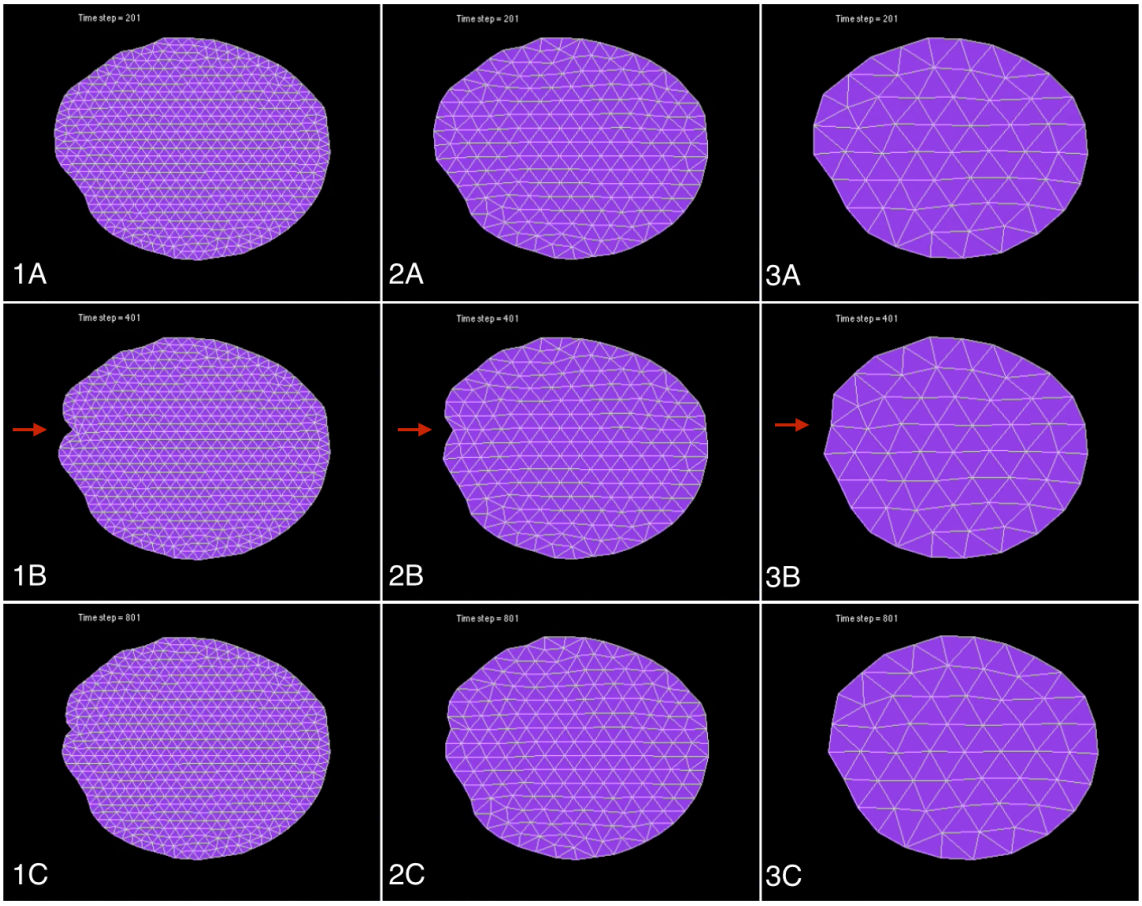

Figure 4.24: The HL60 cell is meshed using three different element size functions and viscoelastic models are created. The resulting viscoelastic models have **(1)** 540 nodes, **(2)** 194 nodes and **(3)** 61 nodes. Simulations are created by applying the same force on three different models. An impulse force is applied on a node (indicated by red arrow) in each case and snapshots of the resulting deformation are shown. **(A)** Before the force is applied. **(B)** Immediately after an impulse force is applied. **(C)** Some time after the force is applied. The cellular model returns to its original shape.

CHAPTER 5

SUMMARY AND FUTURE WORK

5.1 Summary

In this study, computational tools were developed to estimate extracellular and sub-cellular forces in a single cell (or a small population of cells) when it is subjected to external forces such as due to blast waves traversing through tissue and the subsequent formation and rupture of cavitation bubbles. To this effect the ability to capture the shape (or geometry) of cells and nuclei of regular-shaped cells (e.g. HL60 cells) and irregular-shaped cells (e.g. astrocytes) from images was developed. The resulting geometries of the cytoplasm and the nucleus were meshed with different meshing characteristics (different number of mesh points) which were used to create a viscoelastic model of a cell. To create the viscoelastic model, the edges connecting the mesh point were replaced with Voigt elements. An open source software package was developed, which automatically generates a system of coupled ODEs with inequality constraints describing the kinematic response of the viscoelastic model to an external force. A Viscoelastic model of an HL60 cell embedded in an extracellular matrix was developed. The model had 1871 nodes which resulted in a system of 7484 coupled ODEs with inequality constraints. Forces in any part of the model could be estimated as a result of external perturbations. A viscoelastic model for an astrocyte was also developed, although some cell area was lost due to the irregular shape of the astrocyte. An optimization procedure was created to develop the ability to estimate parameters from experimental data. In each case considered, the optimization data (created using parameters from the optimization

procedure) matched the synthetic data (created using known parameters) in at least 50% of the runs, when solving for two Voigt parameters (cytoplasm and nucleus).

5.2 Developing a Multi-scale Model

Using the computational tools developed in this study, forces at the cellular length scale can be estimated. In an experimental setup, cells will be embedded in a collagen-like material (as has been used in similar experimental studies [12]), that will deform following the impact of the incident blast wave. This collagen like material can be modeled using Voigt elements, in a similar way that has been used to model cells in this study (Figure 5.1). Moreover, the Voigt parameters describing this collagen like material can be estimated in a similar way that parameters for the cellular model can be estimated. Given the large number of nodes and the coupled ODEs involved in simulating the coupled viscoelastic model of the material and the cell, a multi-scale modeling strategy can be employed to limit computational expense. To this effect, separate simulations will be developed at different length scales. Using the model of the viscoelastic material, forces can be estimated at the tissue-level length scale and the local force profile around a cell or a group of cells can be determined. This local force profile can be used as external forces (initial condition) for the viscoelastic cell model. Thus forces and associated strain at the cellular length scale can be estimated, by using a multi-scale modeling strategy.

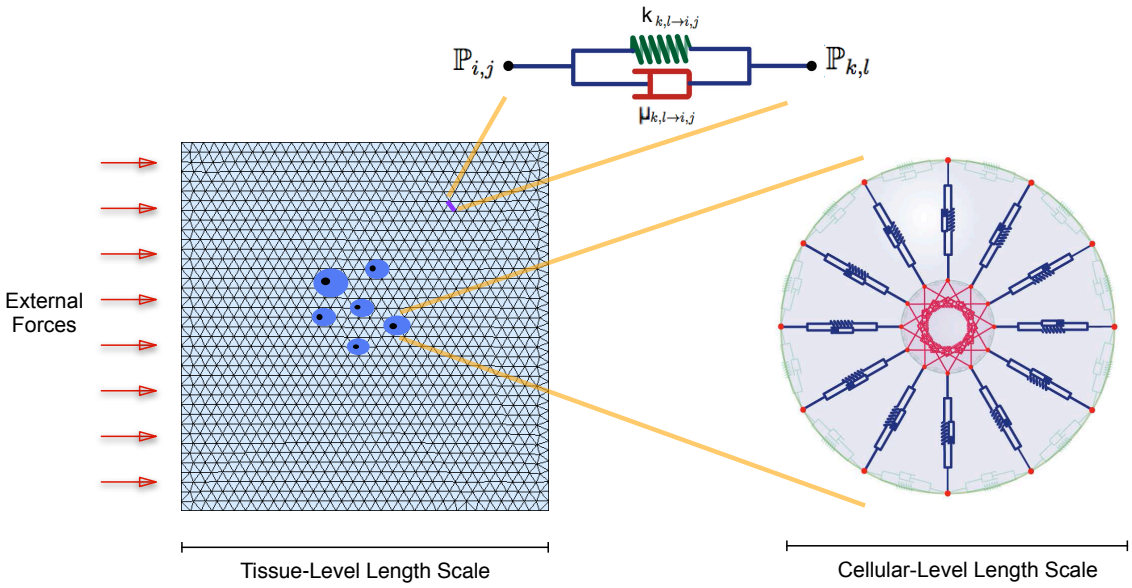

Figure 5.1: Schematic showing the multi-scale modeling strategy. The viscoelastic material in which the cell will be embedded during the experiment will be modeled as a mesh. The nodes are arranged in a triangular mesh where each node $\mathbb{P}_{i,j}$ is connected to another node $\mathbb{P}_{k,l}$ by a Voigt element. A Voigt element is an Hookean spring (purely elastic element) and a Newtonian dashpot (purely viscous element) in parallel. Each Voigt element has a spring constant (k) (units: $\left[1/t^2\right]$), a viscosity parameter (μ) (units: $[1/t]$) and a rest length (l) (units: $[m]$) associated with it. The Voigt element and cellular structure figures are modified from [27].

5.3 Modeling Signal Transduction Networks Using Mass Action Kinetics

Song and Varner [53] developed a mechanistic mathematical model of ATP-induced P2 mediated calcium signaling in archetype sensory neurons. ATP initiates pain by interacting with the P2 family of surface receptors. In their model, they looked at how ATP interacts with ionotropic P2X receptors (ligand gated ion channels) and metabotropic P2Y Gq-protein coupled receptors. Activated P2 receptors are either directly (P2X) or indirectly (P2Y) responsible for the transport of calcium into the cytosol. The model was formulated by gathering molecular modules from literature. Figure 5.2 shows the schematic of the network. They used only mass action kinetics to describe the 90 species connected by 162 interactions and thus the unknown model parameters were either association, dissociation or catalytic rate constants. The model parameters were estimated from experimental data from various laboratories using a multi-objective optimization technique. They were not able to estimate unique model parameters due to the complexity of the model, but instead created an ensemble of probable parameters. In the model, a key interaction specifying how plasma membrane phosphoinositides modulated the activity of P2X channels was hypothesized. Their model quantitatively reproduced experimental measurements from dorsal root ganglion neurons as a function of extracellular ATP forcing (Figure 5.3). Moreover, by performing a sensitivity analysis of the model, they were able to elucidate which molecular subsystems were most important following P2 activation, which may prove useful for the design of the novel pain management strategies.

Sun et al. looked at the effect of externally added ATP on calcium dynamics in neuronal cells [60]. They observed real time intracellular calcium spikes in the neuronal cells using a fluorescent marker. A calcium spike was counted as occurring whenever the intracellular calcium concentration exceeded some set concentration. Figure 5.4 shows the number of calcium spikes against the concentration of ATP added. The calcium spiking activity was enhanced in the presence of ATP $< 0.1\mu M$ but reduced to that found in the normal unexposed cells at higher ATP concentration. The researchers compared their experimental results with simulations of the calcium concentration at three different ATP concentrations using the model developed by Song and Varner (Figure 5.5). They discovered that calcium spiking initially increased as a function of the ATP concentration but beyond a threshold ATP concentration, the calcium spiking was abolished.

Song and Varner created a mathematical model of how a receptor on a membrane is modulated by an external stimulus (ATP), which leads to an influx of calcium in a neuron. This model can be used as a useful starting point to model biological mechanisms in secondary injury following TBI. Instead of P2 receptors induced by ATP, force sensitive receptors induced by forces on the membrane can be modeled. Building a signal transduction network coupled with real time calcium dynamics will lead to a better understanding of the secondary injury following TBI and possible drug development strategies. Moreover, it will help to elucidate the mechanism of mechanosensory transduction molecules.

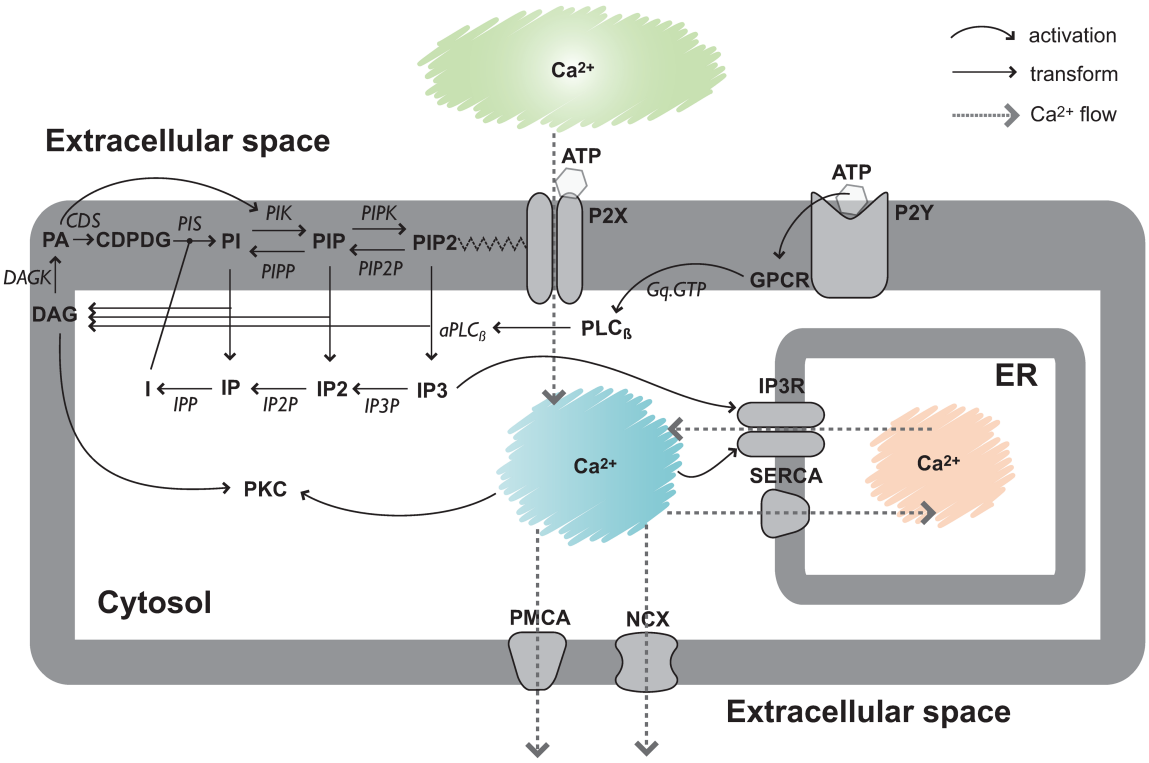

Figure 5.2: Schematic of calcium signaling network. Ca^{2+} can enter the cytosol via P2X channels, inositol trisphosphate receptors (IP3R) and passive Ca^{2+} leakage. ATP binding to P2X activates the channel and induces a rapid increase in cytosolic Ca^{2+} in the presence of extracellular calcium. ATP binding to P2Y receptors activates membrane-bound phospholipase C (PLC) which hydrolyzes phosphatidylinositol-4, 5-bisphophate (PIP2) into inositol 1,4,5-trisphosphate (IP3) and diacylglycerol (DAG). Cytosolic calcium and IP3 binding triggers the opening of IP3R channels and the subsequent release of endogenous Ca^{2+} from the Endoplasmic Reticulum (ER) into the cytosol. Cytosolic Ca is translocated to the extracellular medium by plasma membrane Ca^{2+} ATPase (PMCA) pumps, Na^{+}/Ca^{2+} exchangers (NCX) and to the ER by Sarcoplasmic/Endoplasmic Reticulum Ca (SERCA) ATPase pumps. Phosphoinositides (PIs) are recycled between the plasma membrane and cytosol by phosphorylation and dephosphorylation events. Figure from [53].

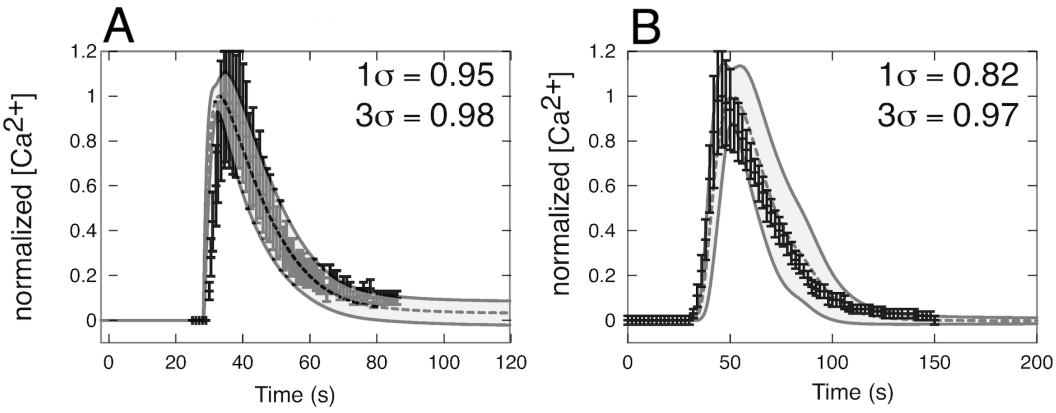

Figure 5.3: Comparison of model simulation versus training data. The dashed lines denote the mean simulated value over the ensemble of model parameters while the shaded regions denote one ensemble standard deviation. Experimental data are shown with error bars. In each corner, the fraction of experimental points captured at one and three standard deviations is given. **(A)** ATP-induced transient increase in cytosolic Ca^{2+} following P2X receptor activation. **(B)** ATP- induced transient increase in cytosolic Ca^{2+} following P2Y receptor activation. Figure is modified from [53].

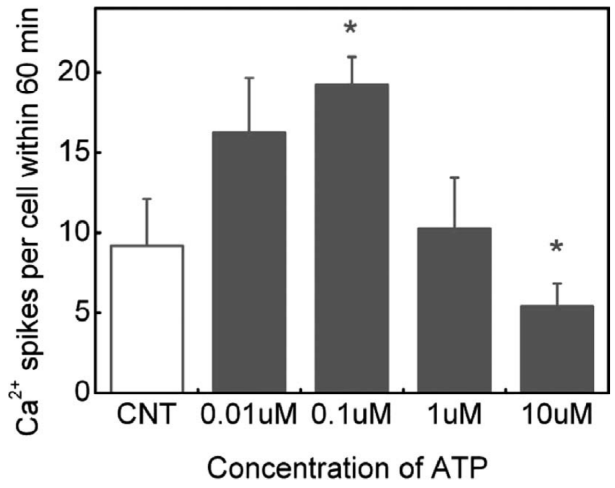

Figure 5.4: Effect of externally added ATP on calcium dynamics in neuronal cells. Figure is modified from [60].

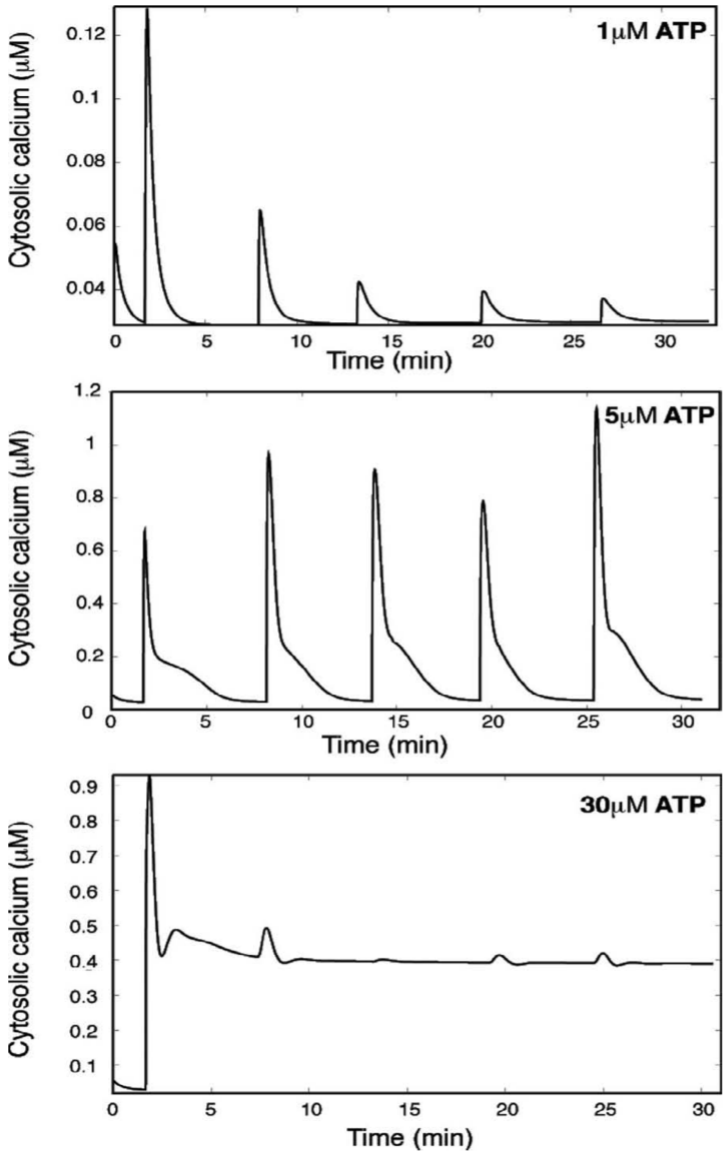

Figure 5.5: Simulation of intracellular calcium dynamics in the presence of extracellular ATP. Figure is modified from [60].

APPENDIX A

SUPPLEMENTAL FIGURES

Figure A.1 show an image of an input file that is input to the Geometry File Generator. It contains the file paths to the mesh-point array, the triangle array, and the destination of the resulting geometry file. Figure A.2 and Figure A.3 show images of a geometry file and a transformation file which are input to the Code Generator. The geometry files describes all the parameters associated with a particular viscoelastic model. The transformation file specifies which language the model equations are to be written in, the input path of the geometry file and the output path for all the files associated with the model equations.

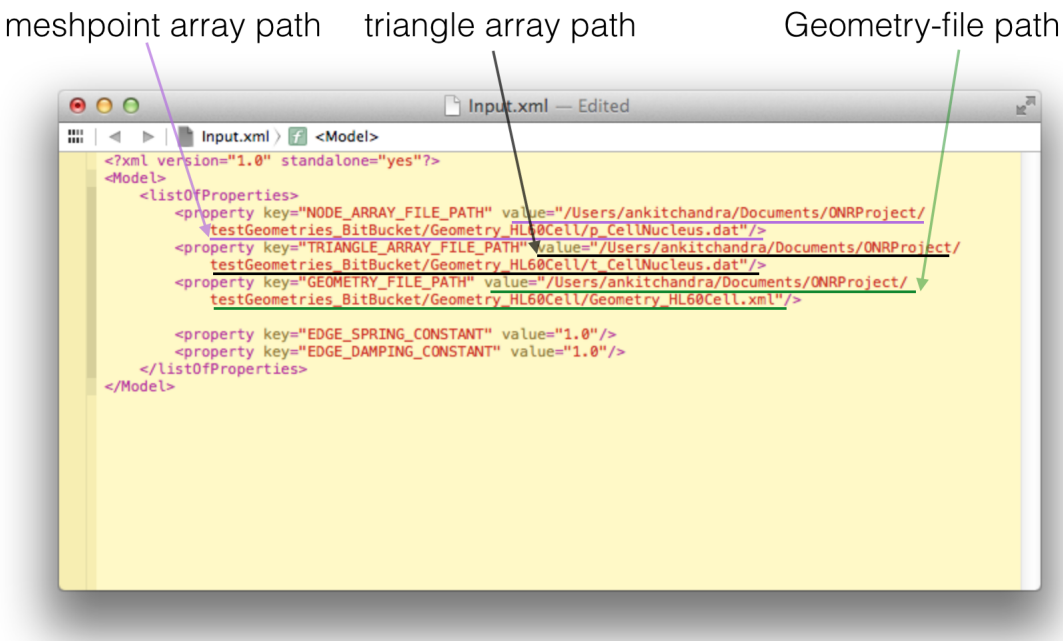

Figure A.1: An image of an input file that contains the file paths to the mesh-point array, the triangle array, and the destination of the resulting geometry file.

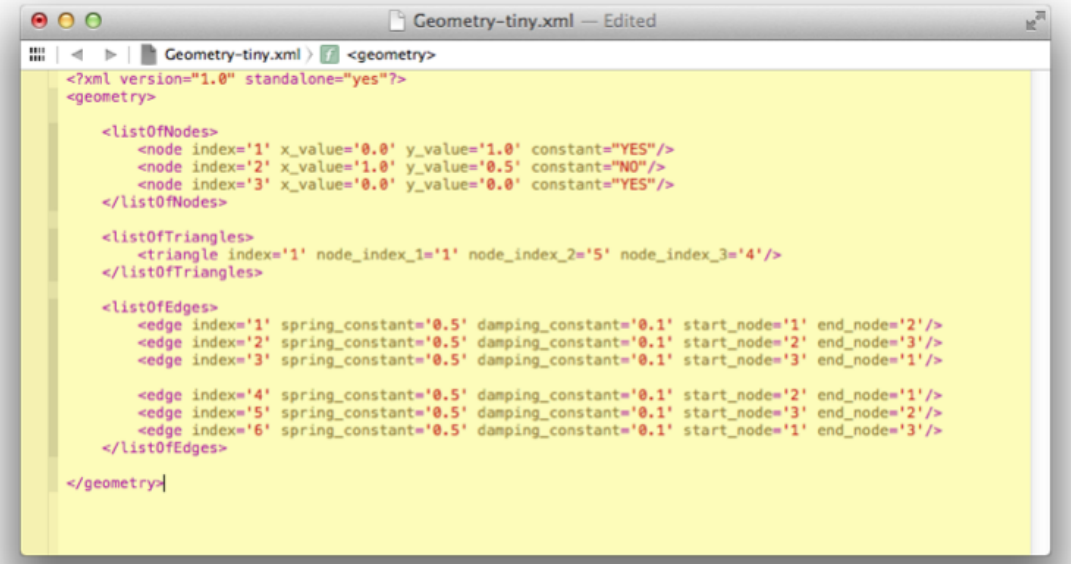

Figure A.2: An image of a geometry file for a simple system consisting of three nodes connected by three Voigt elements. The geometry files describes all the parameters associated with the viscoelastic model.

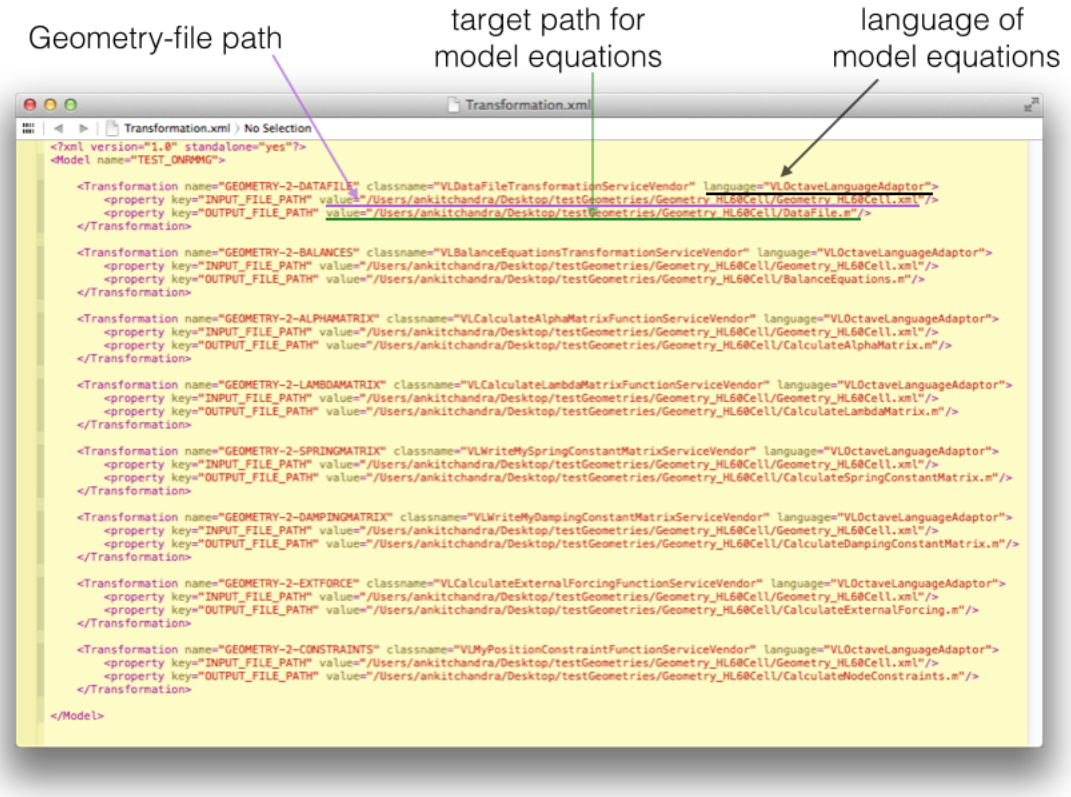

Figure A.3: An image of a typical transformation file. The transformation file specifies which language the model equations are to be written in, the input path of the geometry file and the output path for all the files associated with the model equations.

Figure A.5 and Figure A.4 show plots of dimensionless force on each node in the model (abscissa or x-direction) against dimensionless time for simulations with different damping ratio, ζ, of Voigt elements.

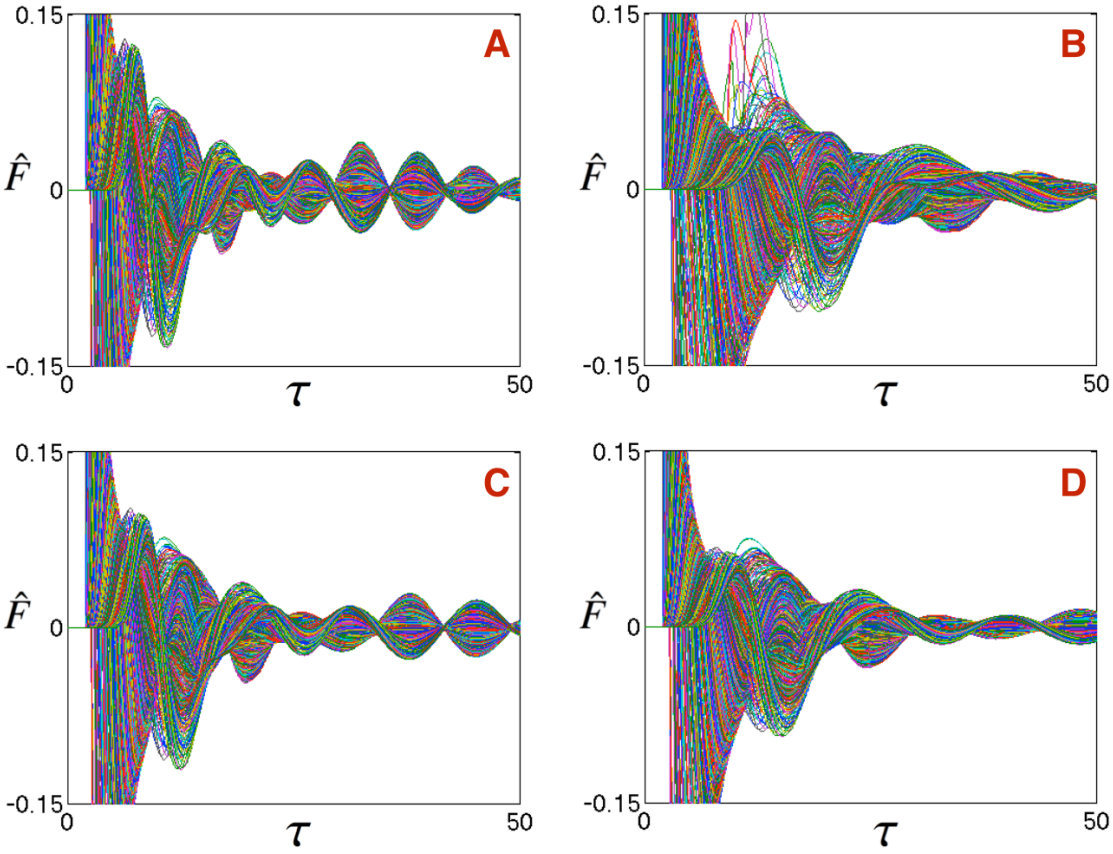

Figure A.4: Dimensionless force (abscissa or x-direction) against dimensionless time for simulations of HL60 cells with different Voigt parameters. A Friedlander force is applied at $\tau = 2$. The cytoplasm and the nucleus had uniform and identical parameters in each case. **(A)** $\mu = 2$, $k = 10$, $\Theta = 0.4$, $\xi = 0.32$. **(B)** $\mu = 1$, $k = 2$, $\Theta = 0.5$, $\xi = 0.35$. **(C)** $\mu = 2$, $k = 7$, $\Theta = 0.57$, $\xi = 0.38$. **(D)** $\mu = 2$, $k = 4$, $\Theta = 1$, $\xi = 0.5$. All parameters are dimensionless.

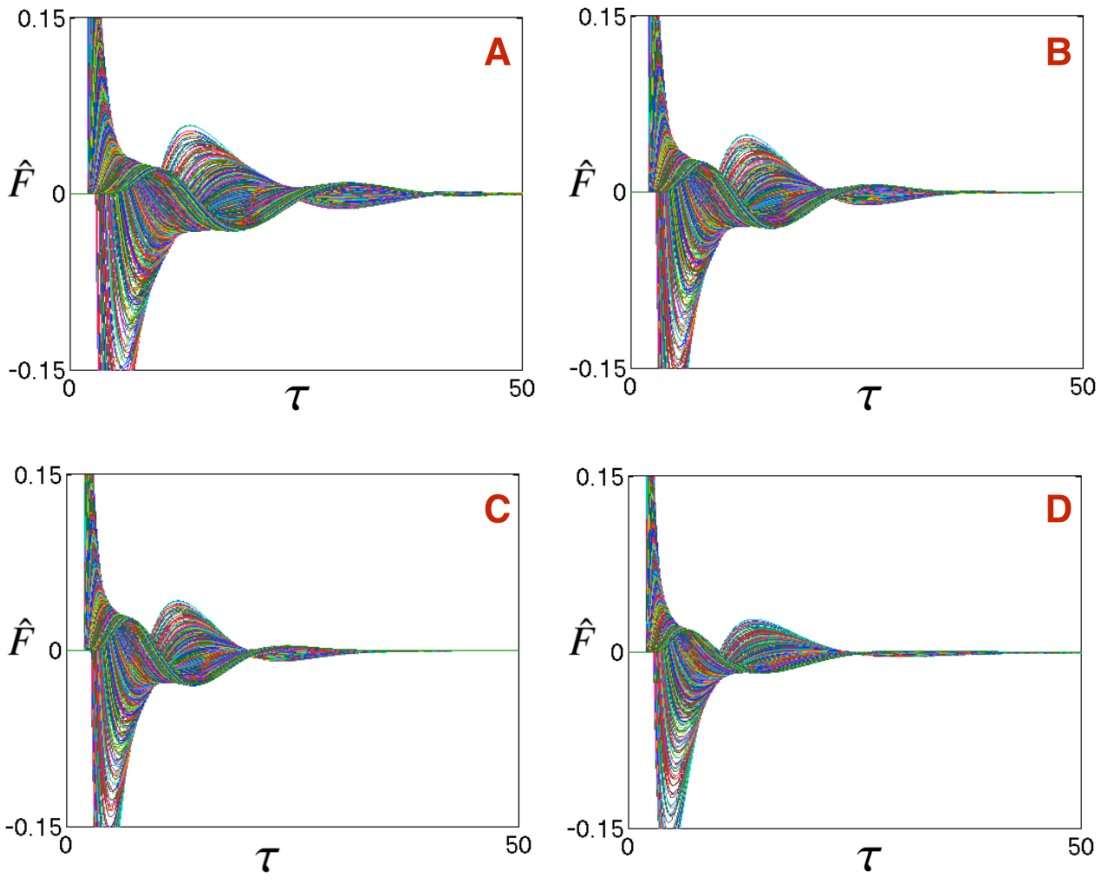

Figure A.5: Dimensionless force (abscissa or x-direction) against dimensionless time for simulations of HL60 cells with different Voigt parameters. A Friedlander force is applied at $\tau = 2$. The cytoplasm and the nucleus had uniform and identical parameters in each case. **(A)** $\mu = 4$, $k = 2$, $\Theta = 8$, $\xi = 1.41$. **(B)** $\mu = 6$, $k = 3$, $\Theta = 12$, $\xi = 1.73$. **(C)** $\mu = 8$, $k = 4$, $\Theta = 16$, $\xi = 2$. **(D)** $\mu = 10$, $k = 2$, $\Theta = 50$, $\xi = 3.54$. All parameters are dimensionless.

BIBLIOGRAPHY

[1] Park E, Bell JD, Baker AJ, "Traumatic Brain Injury: Can the Consequences be Stopped?"*Canadian Medical Association Journal.* **178**, (2008).

[2] Ghajar J, "Traumatic Brain Injury,"*The Lancet.* **356**, (2000).

[3] Sahuquillo J, "Decompressive Craniectomy for the Treatement of Refractory High Intracranial Pressure in Traumatic Brain Injury (Review),"*Cochrane Database of Systematic Reviews.* **1**, (2009).

[4] Warden D, "Military TBI During the Iraq and Afghanistan Wars,"*J Head Truma Rehabil.* **5**, (2006).

[5] Jaffee MS, Helmick KM, Girard PD, Meyer KS, Dinegar K, George K, "Acute clinical care and care coordination for traumatic brain injury within Department of Defense,"*J. Rehabil. Res. Dev.* **46**, (2009).

[6] Okie S, "Traumatic Brain Injury in the War Zone,"*N Eng J Med.* **352;20**, (2005).

[7] Stefanis L, "Caspase-Dependent and ?Independent Neuronal Death: Two Distinct Pathways to Neuronal Injury,"*The Neuroscientist.* **11**, (2005).

[8] Bryan CJ, Clemans TA, "Repetitive Traumatic Brain Injury, Psychological Symptoms, and Suicide Risk in a Clinical Sample of Deployed Military Personnel,"*JAMA Psychiatry.* **1093**, (2013).

[9] Cho Lab, *Bioengineering Department, University of Illinois at Chicago.*

[10] Bryan CJ, Clemans TA, Hernandez AM, Rudd MD, "Loss of consciousness, Depression, Posttraumatic Stress Disorder, and Suicide Risk Among Deployed Military Personnel With Mild Traumatic Brain Injury,"*J Head Trauma Rehabil.* **28**, (2013).

[11] Tolias CM, Bullock RM, "Critical Appraisal of Neuroprotection Trials in Head Injury: What Have We Learned?"*The Journal of the American Society for Experimental NeuroTherapeutics.* **1**, (2004).

[12] Sarntinoranont M, Lee SJ, Hong Y, King MA, Subhash G, Kwon J, Moore DF, "High Strain Rate Brain Injury Model Using Submerged Acute Rat Brain Tissue Slices,"*Journal of Neurotrauma.* **29**, (2012).

[13] Chen YC, Smith DH, Meaney DF, "*In-Vitro* Approaches fro Studying Blast-Induced Traumatic Brain Injury,"*Journal of Neurotrauma.* **26**, (2009).

[14] Nishimura N, Schaffer CB, Friedman B, Tsai PS, Lyden PD, Kleinfeld D, "Targeted insult to subsurface cortical blood vessels using ultrashort laser pulses: three models of stroke,"*Nat Methods.* **3**, (2006).

[15] Vogel A, Noack J, Huttman G Paltauf G, "Mechanisms of femtosecond laser nano surgery of cells and tissues,"*Appl. Phys. B.-Lasers O.* **81**, (2005).

[16] Yanik MF, Cinar H, Cinar HN, Chisholm AD, Jin YS, Ben-Yakar A, "Neurosurgery-Functional regeneration after laser axotomy,"*Nature.* **432**, (2004).

[17] Wiesner TF, Berk BC, Nerem RM, "A mathematical model of the cytosolic-free calcium response in endothelial cells to fluid shear stress,"*Proc. Natl. Acad. Sci. USA.* **94**, (1997).

[18] Charles AC, Merrill JE, Dirksen ER, Sanderson MJ, "Intercellular Signaling in Glial Cells: Calcium Waves and Oscillations in Response to Mechanical Stimulation and Glutamate,"*Neuron.* **6**, (1991).

[19] Davies PF, "Flow mediated endothelial mechanotransduction,"*Physiol Rev.* **75**, (1995).

[20] Dewey CF Jr., Bussolari SR, Gimbrone MA Jr., Davies PF, "The dynamic response of vascular endothelial cells to fluid shear stress,"*J. Biomech. Eng.* **103**, (1981).

[21] Gimbrone MA Jr., Topper JN, Nagel T, Anderson KR, Garcia-Cardeña G, "Endothelial dysfunction, hemodynamic forces and atherogenesis,"*Ann. N Y Acad. Sci.* **902**, (2000).

[22] Lehoux S, Tedgui A, "Cellular mechanics and gene expression in blood vessels,"*J Biomech.* **36**, (2003).

[23] McCormick SM, Frye SR, Eskin SG, Teng CL, Lu CM, Russel CG, Chittur KK, McIntire LV,"Microarray analysis of shear stressed endothelial cells,"*Biorheology.* **40**, (2003).

[24] Kamm RD, Mofrad MRK,"Introduction, with the biological basis for cell

mechanics,"*Cytoskeletal Mechanics. Models and Measurements.* Cambridge University Press (2006).

[25] Jamison CE, Marangoni RD, Glaser AA, "Viscoelastic Properties of Soft Tissue by Discrete Model Characterization,"*J. Biomechanics.* **1**, (1968).

[26] Ghadiali S N, Dailey H L "Mechanobiology and Finite Element Analysis of Cellular Injury During Microbubble Flows,"*Stud Mechanobiol Tissue Eng Biomater.* **4**, (2011).

[27] Jamali Y, Azimi M, Mofrad MRK, "A Sub-Cellular Viscoelastic Model for Cell Population Mechanics,"*PLOS ONE* **5**, (2010).

[28] Karcher H, Lammerding J, Huang H, Lee RT, Kamm RD Kaazempur-Mofrad MR, "A Three-Dimensional Viscoelastic Model for Cell Deformation with Experimental Verification,"*Biophysical Journal* **85**, (2003).

[29] Bausch AR, Ziemann F, Boulbitch A, Jacobson K, Sackmann E, "Local measurements of viscoelastic parameters of adherent cell surfaces by magnetic bead microrheology,"*Biophysical J.* **75**, (1998).

[30] Evans E, "Bending elastic modulus of red blood cell membrane derived from buckling instability in micropipette aspiration tests,"*Biophysical J.* **43**, (1983).

[31] Yamada S, Wirtz D, Kuo SC, "Mechanics of living cells measured by laser tracking microrheology,"*Biophysics J.* **78**, (2000).

[32] Paszek MJ, Boettiger D, Weaver VM, Hammer DA, "Integrin Clustering Is Driven by Mechanical Resistance from the Glycocalyx and the Substrate,"*PLOS Computational Biology.* **5**, (2009).

[33] Darvish KK, Crandall JR, "Nonlinear Viscoelastic Effects in Oscillatory Shear Deformation of Brain Tissue,"*Medical Engineering & Physics.* **23**, (2001).

[34] Sanjeevi R, "A Viscoelastic Model for the Mechanical Properties of Biological Materials,"*J. Biomechanics.* **15**, (1982).

[35] Sanjeevi R, Somanathan N, Ramaswamy D, "A Viscoelastic Model for Collagen Fibres,"*J. Biomechanics.* **1**, (1982).

[36] Prevost TP, Balakrishnan A, Suresh S, Socrate S, "Biomechanics of Brain Tissue,"*Acta Biomaterialia.* **7**, (2011).

[37] Wang N, Tytell JD, Ingber DE, "Mechanotransduction at a Distance: Mechanically Coupling the Extracellular Matrix with the Nucleus,"*Nature Review Molecular Cell Biology.* **10**, (2009).

[38] Vogel V, Sheetz M, "Local force and geometry sensing regulate cell functions,"*Nature Review Molecular Cell Biology.* **7**, (2006).

[39] Margadant F, Chew LL, Hu X, Yu H, Bate N, "Mechanotransduction In Vivo by Repeated Talin Stretch Relaxation Events Depends upon Vinculin,"*PLOS Biol.* **9**, (2011).

[40] Chalfie M, "Neurosensory Mechanotransduction,"*Nature Reviews Molecular Cell Biology.* **10**, (2009).

[41] Kung C, "A Possible unifying principle for mechanotransduction,"*Nature.* **436**, (2005).

[42] Sukharev S, Betanzos M, Chiang CS, Guy RH, "The gating mechanism of the large mechanosensitive channel MscL,"*Nature.* **409**, (2001).

[43] Gillespie PG, Walker RG "Molecular Basis for Mechanosensory Transduction,"*Nature.* **413**, (2001).

[44] O'Hagan R, Chalfie M, Goodman MB, "The MEC-4 DEG/ENaC Channel of Caenorhabditis Elegans Touch Receptor Neurons Transduces Mechanical Signals,"*Nature Neurosci.* **8**, (2005).

[45] Walker RG, Willingham AT, Zuker CS, "A Drosophila Mechanosensory Transduction Channel,"*Science.* **287**, (2000).

[46] Kernan M, Cowan D, Zuker C, "Genetic Dissection of Mechanosensory Transduction: Mechanoreception-defective Mutations of Drosophila,"*Neuron.* **12**, (1994).

[47] Maxwell WL, Povlishock JT, Graham DL, "A Mechanistic Analysis of Nondisruptive Axonal Injury: A Review,"*J. Neurotrauma.* **14**, (1997).

[48] Saelens X, Festjens N, Walle LV, VanGurp M, VanLoo G, Vandenabeele P,

"Toxic Proteins Released from Mitochondria in Cell Death,"*Oncogene.* **23**, (2004).

[49] Dawson VL, Dawson TM, "Deadly Conversations: Nuclear-Mitochondrial Cross-Talk,"*J. Bioenerg Biomembr.* **36**, (2004).

[50] Zadeh LA, "Fuzzy Logic = Computing with Words,"*IEEE Transactions on Fuzzy Systems.* **4**, (1996).

[51] Aldridge BB, Saez-Rodriguez J, Muhlich JL, Sorger PK, Lauffenburger DA, "Fuzzy Logic Analysis of Kinase Pathway Crosstalk in TNF/EGF/Insulin-Induced Signaling,"*PLOS Computational Biology.* **5**, (2009).

[52] Morris MK, Saez-Rodriguez J, Clarke DC, Sorger PK, Lauffenburger DA, "Training Signaling Pathway Maps to Biochemical Data with Constrained Fuzzy Logic: Quantitative Analysis of Liver Cell Responses to Inflammatory Stimuli,"*PLOS Computational Biology.* **7**, (2011).

[53] Song SO & Varner JD, "Modeling and Analysis of the Molecular Basis of Pain in Sensory Neurons,"*PLOS ONE.* **4**, (2009).

[54] Lequieu J, Chakrabarti A, Nayak S, Varner JD, "Computational Modeling and Analysis of Insulin Induced Eukaryotic Translation Initiation,"*PLOS Computational Biology.* **7**, (2011).

[55] Persson P, Strang, G, "A Simple Mesh Generation in Matlab,"*http://persson.berkeley.edu/distmesh/persson04mesh.pdf.* online.

[56] Persson P "Mesh Generation for Implicit Geometries," *Ph.D. thesis, Department of Mathematics, MIT.* (2004).

[57] Provot X, "Deformation Constraints in a Mass-Spring Model to Describe Rigid Cloth Behavior,"*Graphics Interface.* **1**, (1995).

[58] Mosegaard J, "Cardiac Surgery Simulation,"*PhD Dissertation - University of Aarhus.* (2006).

[59] Coskun H, Yi L, Mackey MA, "Ameboid Cell Motility: A Model and Inverse Problem, with an Application to Live Cell Imaging Data,"*Journal of Theoretical Biology.* **244**, (2007).

[60] Sun S, Titushkin I, Varner JD, Cho M, "Millimeter Wave-Induced Modulation of Calcium Dynamics in an Engineered Skin Co-Culture Model: Role of Secreted ATP on Calcium Spiking,"*J. Radiat. Res.* **53**, (2012).

[61] Chan TF, Vese LA, "Active Contours without Edges,"*IEEE Transactions on Image Processing.* **10**, (2001).

[62] Mumford D, Shah J, "Optimal approximation by piecewise smooth functions and associated variational problems,"*Commun. Pure Appl. Math.* **42**, (1989).

[63] Chandra N, Ganpule S, Kleinschmit, Feng R, Holmberg AD, Sundaramurthy, Selvan V, Alai A, "Evolution of blast wave profiles in simulated air blasts: experiment and computational modeling,"*Shock Waves.* **22**, (2012).

[64] Nakagawa A, Manley GT, Gean AD, Ohtani K, Armonda R, Tsukamoto A, Yamamoto H, Takayama K, Tominaga T, "Mechanisms of Primary Blast-Induced Traumatic Brain Injury: Insights from Shock-Wave Research,"*Journal of Neurotrauma.* **28**, (2011).